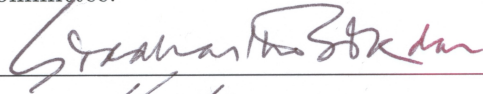# SEMIAUTOMATIC SEGMENTATION OF ATHEROSCLEROTIC CAROTID ARTERY WALL USING 3D ULTRASOUND IMAGING

by

Md Murad Hossain
A Thesis
Submitted to the
Graduate Faculty
of
George Mason University
In Partial fulfillment of
The Requirements for the Degree
of
Master of Science
Electrical Engineering

Committee:

Dr. Siddhartha Sikdar, Thesis Director

Dr. Kenneth J. Hintz, Committee Member

Dr. Vasiliki Ikonomidou, Committee Member

Dr. Andre Manitius, Department Chairman

Dr. Kenneth S. Ball, Dean,
Volgenau School of Engineering

Date: 05 /01 /2014

Spring Semester 2014
George Mason University
Fairfax, VA

Semiautomatic Segmentation of Atherosclerotic Carotid Artery
Wall Using 3D Ultrasound Imaging

A thesis submitted in partial fulfillment of the requirements for the degree of
Master of Science at George Mason University

By

Md Murad Hossain
Bachelor of Science
Islamic University of Technology, Bangladesh, 2009

Director: Dr. Siddhartha Sikdar, Assistant Professor
Department of Electrical and Computer Engineering

Spring Semester 2014
George Mason University
Fairfax, VA

Dedication

To you
who through your support, love, and criticism
enables me to go forward and remain standing

Acknowledgments

I would like to thank God for keeping me safe and sound from 8082 miles away from my home.

I would like to thank Dr. Siddhartha sikdar for his tireless guidance and supports in my research. He patiently listened all my complains. He introduced me to the interesting field of medical image processing and ultrasound imaging. He gave me the motivation what i have today.

I would like to thank Dr. Brajesh K. Lal for his clinical input in this work and to all the project members in the "Asymptomatic Carotid Stenosis: Cognitive Function and Plaque Correlates (ACCOF)" projects for interesting discussion about the project. Special thanks to Limin, Greg, and Khalid for collecting patients data.

I am greatly thankful to my parents, sisters, and friends for their support during my MS in a foreign land and in a different culture.

Table of Contents

List of Tables

List of Figures

Abstract

SEMIAUTOMATIC SEGMENTATION OF ATHEROSCLEROTIC CAROTID ARTERY WALL USING 3D ULTRASOUND IMAGING

Md Murad Hossain, MS

George Mason University, 2014

Thesis Director: Dr. Siddhartha Sikdar

Stroke is an interruption of blood to any part of the brain. It is the fourth leading cause of death in the USA. Rupture of atherosclerotic plaques in the carotid artery has been implicated in 20% of strokes. Currently, severity of plaques is assessed by measuring the velocity of blood flow through the stenosed artery using Doppler ultrasound. However, imaging and monitoring plaque progression in 3D can better classify disease severity and potentially identify plaque vulnerability to rupture. Vessel wall volume (VWV) has been proposed as a 3D measurement of arterial wall and plaque burden. It is defined as the enclosed volume between the adventitial wall boundary (AWB) and the lumen-intima boundary (LIB). A computer-based algorithm for the segmentation of LIB and AWB will accelerate the translation of VWV of carotid atherosclerosis to clinical research and clinical practice. The goal of this thesis is to develop semi-automatic 2D and 3D segmentation algorithms for segmenting LIB and AWB of the carotid artery from proximal common carotid to distal internal and external carotid artery.

Our proposed segmentation algorithm uses distance regularized level set method with edge-based energy, region-based energy, smoothness energy, and a novel stopping criteria to segment LIB and AWB of carotid artery from 3D US images. 3D US images were   acquired

from patients with asymptomatic carotid plaques as part of an ongoing clinical study. The data set consists of 210 2D cross-sectional slices selected from 10 3D US patient images at an inter-slice distance of 1 mm. Manual initialization at an inter slice distance of 4 mm was used. To stop the leaking of evolving contour through the poor boundary contrast regions, we defined a stopping boundary (2D algorithm) or surface (3D algorithm) based energy. To save computational time, change of modified Hausdorff distance (MHD) between evolving contours at successive iterations (2D algorithm) or percentage change of pixel locations (3D algorithm) was used as stopping criteria along with stopping boundary or surface based energy. Due to the absence of clinical ground truth boundary, an average curve was generated from manually segmented boundaries by three observers. The average curve was used as a ground truth boundary and algorithm generated boundary was compared against it. The error metrics are dice similarity coefficient (DSC), Hausdorff distance (HD), and MHD.

The proposed stopping criteria were compared with other two conventional stopping criteria: percentage change of area inside evolving contours and change of MHD between evolving contours at successive iterations. The performance of the proposed algorithm was better than other two stopping criteria and yielded mean of: LIB_{DSC}=88.78%, $\text{AWB}_{DSC} = 94.81\%$, LIB_{MHD}=0.26 mm, AWB_{MHD}=0.25 mm, LIB_{HD}=0.74 mm, AWB_{HD}=0.80 mm. The Bland-Altman plot and correlation coefficient ($r = 0.99$) indicated a high agreement between ground truth boundaries and algorithm generated boundaries. The minimum detectable change of VWV by the proposed algorithm is 10.89 % (2D) and 11.22 %(3D) of average volume. The overall execution time to segment whole volume is 40 ± 5 min and 100 ± 5 min for algorithm and manual observers respectively. Preliminary validation on 10 subjects showed that the algorithm accurately segmented LIB and AWB. Our method can be helpful in clinical care for fast and economical monitoring of 3D plaque progression and regression during therapy.

Chapter 1: Introduction

Computer aided diagnosis (CAD) is a procedure of assisting clinicians to interpret medical images. Manual extraction of quantitative biological markers from medical images is time-consuming and tedious. It also suffers from intra- and inter- observer variability. Signal processing, image analysis, and pattern recognition tools have been used to extract biological markers from medical images which were previously considered intractable. Delineating a region of interest is one of the main steps in computer assisted quantification and interpretation of medical images. Outlining regions by means of automatic/ semiautomatic segmentation algorithm has the potential to reduce tedious manual outlining and leads to better utilization of an expert clinician's time. It also has the potential to reduce inter- and intra-observer variability.

1.1   Stroke

Stroke is an interruption of blood supply to a part of the brain. It represents the third most common cause of death in world [2] and fourth most common cause of death in the USA [3]. According to the World Health Organization, 15 million people suffer stroke worldwide annually. 5 million die, and another 5 million are permanently disabled out of these 15 million people. About 795,000 people suffer from stroke, and 143,579 people die from stroke annually in the United States [4, 5].

There are two types of stroke: ischemic and hemorrhagic. Hemorrhagic strokes occur due to the breakage of a blood vessel in the brain and ischemic strokes occur due to blockage of a blood vessel in the brain by atheroembolic or thromboembolic debris originated from the other parts of the body. Approximately 85% of all strokes are ischemic strokes [6, 7].

1.2   Atherosclerotic Carotid Artery

Atherosclerosis is a chronic, systemic, inflammatory disease of the medium and large arteries. Atherosclerotic plaques are defined by intimal thickening that occurs due to the progressive accumulation of lipids [8] together with numerous cellular and molecular components such as smooth muscle cells , lipid-filled macrophages, monocytes, T and B lymphocytes, erythrocytes, and platelets [9, 10]. It causes stenosis (i.e., narrowing) of the blood vessel and embolisms. 20% of ischemic strokes are due to the atherosclerotic plaques in the carotid artery [6, 7].

Carotid arteries supply blood to the brain and face. The common carotid artery (CCA) bifurcates into the internal carotid artery(ICA), and the external carotid artery (ECA) (figure 1.1,figure 1.5). The ICA supplies blood to brain where as the ECA supplies blood to face, scalp, and neck. The frequency of carotid plaque formation at the bifurcation region is very high due to the disturbance of laminar blood flow and low shear stress at carotid bifurcation [11]. Blood flow becomes more turbulent with increasing degree of stenosis in the ICA, resulting in escalation of atheroembolization [11].

1.3   Quantitative Assessment of Carotid Plaque

Carotid Endarterectomy (CEA) is an invasive treatment for atherosclerotic carotid artery that has been widely advocated as a stroke prevention measure . It is a surgical procedure to remove plaque from carotid arteries as shown in figure 1.1. The North American Symptomatic Carotid Endarterectomy Trial (NASCET) and the European Carotid Surgery Trial (ECST) showed that patients with high grade ($\geq$ 70%) ICA stenosis benefited from the CEA compared with the group receiving conservative treatment [12–15]. The Asymptomatic Carotid Atherosclerosis Study (ACAS) showed a 5.8% risk reduction of stroke at 5 years after CEA in patients with asymptomatic high-grade carotid stenosis ($\geq$ 60%). They concluded that CEA was beneficial when performed in centers where morbidity and mortality were 3% or less[16–18]. There is a debate about the criteria for selecting asymptomatic ICA stenosis patients for CEA and risk stratification is necessary to identify these patients [16, 19].
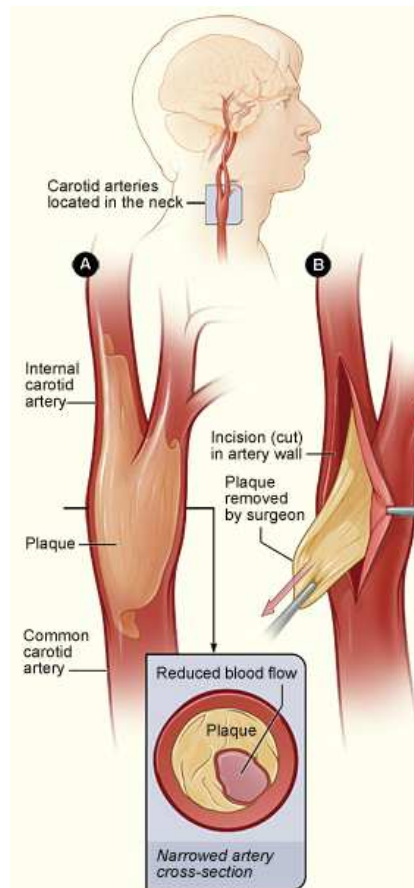
Figure 1.1: Location of carotid artery and process of carotid endarterectomy. Figure A shows different carotid artery with plaque buildup and an inset image of a cross-section of the narrowed carotid artery due to plaque. Figure B shows the process of carotid endarterectomy i.e., removal of the plaque. Public domain image and selected text provided courtesy of The National Heart, Lung, and Blood Institute `http://www.nhlbi.nih.gov/health/health-topics/topics/catd/treatment.html`

Quantitative assessment of plaque offers the advantage of monitoring plaque stabilization by drug therapies. It also helps to select those patients with high risk plaques so they can be treated with CEA while the vast majority of patients with low risk plaques can be treated medically.

Indirect physiologic measurements such as blood pressure or cholesterol levels can provide indication of atherosclerosis [11]. However, these measurements can not be isolated as causes of carotid artery atherosclerosis. Contrary to these indirect measurements, medical imaging techniques provide ways to examine the plaque anatomy directly.

Angiography is a way of visualizing blood vessels by injection of a contrast agent into the
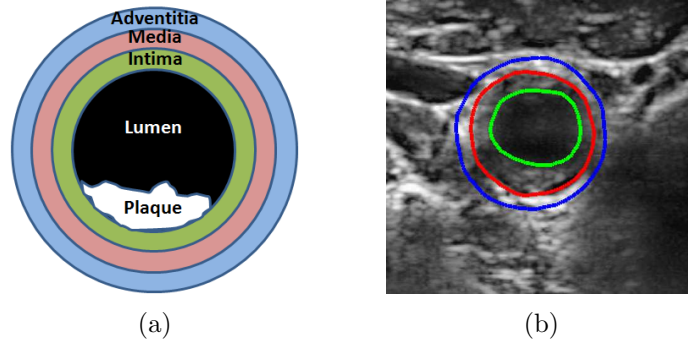
Figure 1.2:   a) Schematic cross section of carotid artery shows intima, media, and adventitia layers of carotid artery b) Manually delineated lumen-intima boundary (green), media-adventitia boundary (red), and adventitial wall boundary (blue) on a 2D cross-sectional US image.

bloodstream. Computed tomography (CT) angiography (CTA) gives a three-dimensional image of blood vessel by taking a series of x-ray images at regular angles and is used to identify atherosclerotic plaque in the carotid bifurcation region [20]. Although it is widely available and cost-effective, it exposes the patient to a significant dose of ionizing radiation and iodine-based contrast agent may cause allergic reaction to the patient [20]. It is recommended to use CTA only in life-threatening cases or severe stenosis patients. Magnetic resonance imaging (MRI) provides high quality images of blood vessels and is used to measure arterial wall thickness [21] and plaque composition [22]. The main drawback of MRI is its comparatively high cost which prohibits the use of MRI as a screening tool for asymptomatic stroke patients.

Duplex ultrasonography is the most widely used screening tool to evaluate atherosclerotic plaque and stenosis of the carotid artery for asymptomatic stroke patients due to its cost-effectiveness, non-invasiveness, and portability. It is commonly used to monitor asymptomatic stroke patients serially for progression of disease or after carotid endarterectomy. Visualization of intima, media, and adventitia layer (figure 1.2a) of carotid artery and assessment of arterial wall changes with precise measurements in 3D are possible due to novel ultrasonic imaging techniques. Figure 1.2b shows manually delineated adventitial wall boundary (blue), media-adventitia boundary (red), and lumen-intima boundary (green)
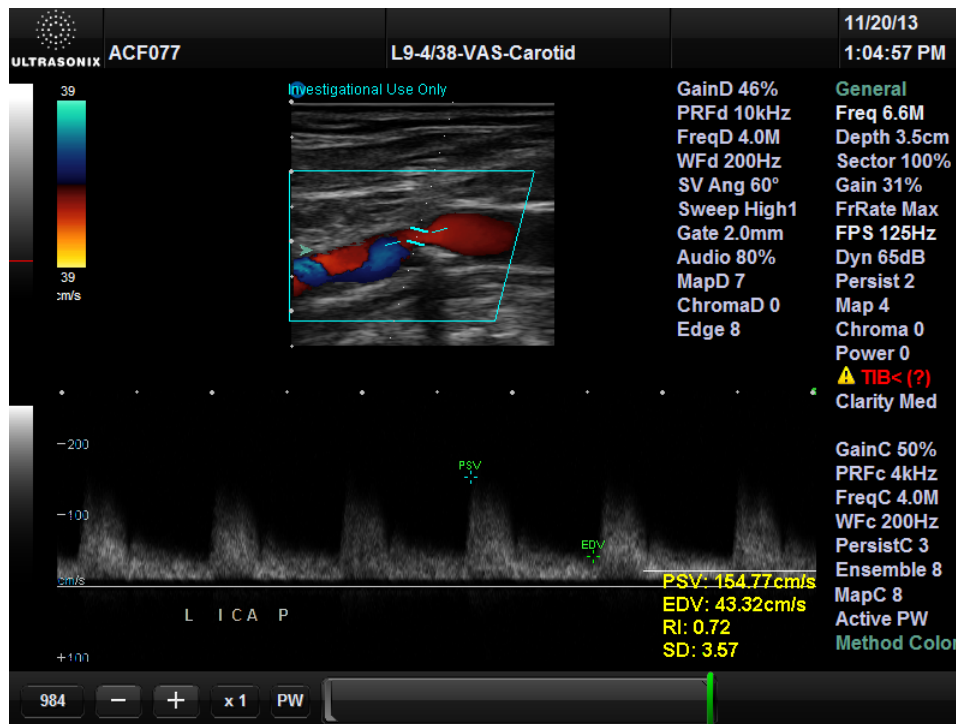
Figure 1.3: Ultrasonic duplex Doppler velocity measurements at stenosed region of ICA. The patient has moderate stenosis (50%-69%) based on Peak systolic velocity (PSV) (154.77 *cm/s*) and end diastolic velocity (EDV)(43.32 *cm/s*).

on a 2D cross-sectional US image.

The established quantitative assessment of carotid stenosis is ultrasonic duplex Doppler velocimetry [23]. Color Doppler sonography allows simultaneous real-time visualization of vascular lesions and associated flow abnormalities. The color Doppler sonography aids sonographer to find the origin of ICA and stenosed regions. The cursor is placed in the center of the carotid lumen at an angle of 60^0 or less on the B-mode gray scale image for Doppler spectral display (figure 1.3). The highest velocity is detected after sampling through the whole stenosis region. The main limitation of Doppler velocity measurement is that it showed a considerable spread of values relative to angiographic stenosis percentage [24]. This means that a wide range of associated blood flow velocities is recorded for any given degree of angiographic stenosis. It affects the sensitivity and specificity of the sonographic tests. It also strongly affects the positive and negative predictive values. There is no validation data that directly relate carotid velocities to patients benefits from CEA.

Tortuosity of the ICA due to kinking and coiling secondary to atherosclerosis may increase peak systolic velocity (PSV) in the ICA.

Due to the limitations of ultrasonic duplex Doppler velocimetry method, other ultrasonic imaging measurements for quantifying carotid atherosclerosis have been proposed in the literature. The established ultrasonic imaging based quantitative measurement is IMT (one dimensional measurement of thickness of intima and media figure 1.2) [25]. Though, IMT has been shown to correlate with vascular outcomes [26], it may reflect many distinct biological pathways and mechanisms like hypertensive medial hypertrophy [27] or compensatory intimal thickening due to mechanical forces of blood flow [28]. More recently, total plaque area(TPA) [29] and total plaque volume (TPV) [30] have emerged as complementary ultrasonic phenotypes of carotid atherosclerosis which provide quantitative measurements of plaque burden in two dimensions (2D) and three dimensions (3D), respectively. TPA is generally measured from a plane which contains the most plaque. However, plaque grows in three dimensions and any 1D or 2D measurements are unable to capture global change in plaque. TPV is calculated by segmenting the plaque boundary in all cross sectional slices that contain plaques. Though TPV provides global plaque burden in 3D, it suffers from large intra- and inter- observers variability, long training times for observers and long duration to perform manual segmentations because it is difficult to distinguish vessel wall from plaque in 3D US images. In order to overcome some of these limitations and accelerate the translation of 3D measurements of carotid atherosclerosis to clinical research and clinical practice, vessel wall volume (VWV) [31,32] was proposed as new 3D measurements of plaque burden. VWV is a 3D measurements of vessel wall thickness and plaque. It can be measured by segmenting adventitial wall boundary (AWB) or media-adventitia boundary (MAB) and lumen-intima boundary (LIB) (figure 1.2b).We hypothesize that there is a possibility of missing plaque in the calculation of VWV if MAB is segmented as an outer boundary. AWB measurement is more reproducible than MAB measurement because it becomes difficult to distinguish media from adventitia with presence of plaque in US images.

1.4 Literature Review

In this section, existing approaches for the calculation of VWV from the US images will be presented. We will also discuss the limitations of existing approaches. Due to the nature of US images, there is a possibility of over-segmentation. We will also present existing approaches, used in the segmentation algorithm to stop over-segmentation and their limitations. This section is divided into two parts: arterial wall segmentation for the calculation of VWV (section 1.4.1) and stopping criteria for correct boundary segmentation (section 1.4.2) .

1.4.1 Arterial Wall Segmentation for the Calculation of VWV

Though it has been reported that VWV changes more than IMT over time, VWV has not been used clinically due to the lack of a fast, accurate and reproducible tool to segment AWB/MAB and LIB [33]. Several investigations have been reported on manual segmentation of carotid artery wall by expert observers [34–36]. However, manual segmentation is labor-intensive and time consuming and it also suffers from inter- and intra-observer variability. 2D and 3D automatic and semi automatic algorithms are reported to segment LIB or/and MAB on 2D/3D US [33, 37–46].

The existing algorithms can be divided into two main categories: algorithms only segmented carotid lumen [37–39, 41, 42, 46] and algorithms segmented both carotid LIB and MAB/AWB [33, 43–45]. Each category can be divided into two classes: algorithms segmented only common carotid artery [33, 37–45] and algorithms segmented both common and internal carotid artery [46].

Gill *et al.*[40], Solovey [42], and Lorza *et al.* [46] proposed direct 3D methods for lumen segmentation of CCA, ICA and ECA. Gill *et al.* [40] used a 3D dynamic balloon model to locate the luminal boundary which is refined by edge-based energy. However, edge-based energy will not able to stop leaking through shadowing region figure 1.4c or missing boundary region figure 1.4b. Solovey [42] incorporated *Bhattacharyya* regional

Table 1.1: Summary of existing algorithms for segmenting carotid LIB/AWB/MAB from Ultrasound images. (ISD=inter-slice distance, LIB=Lumen-intima boundary, MAB=Media-adventitia boundary, AWB=Adventitial wall boundary, CCA= common carotid artery, ICA= internal carotid artery, and ECA= external carotid artery.)

Paper	Year	Dime-nsion	LIB	MAB/ AWB	Carotid Artery Type	No. of images (type)	Manual works
Ukwatta [45]	2013	3D	Sparse field level sets	Sparse field level sets	CCA	21 (3D)	Anchor points on the boundary slice at ISD 3mm
Lorza [46]	2013	3D	Surface Graph Cuts	No	CCA, ICA, ECA	3 (3D)	Seed points at beginning of CCA, ICA, and ECA
Yang [44]	2012	2D	Active shape model	Active shape model	CCA	68 (3D)	Requires a shape model on each slice and training data
Ukwatta [43]	2011	2D	Coupled level set	Coupled level set	CCA	21 (3D)	Anchor points on the boundary slice at ISD 1mm
Ukwatta [33]	2011	2D	Level set	Level set	CCA	21 (3D)	Anchor points on the boundary slice at ISD 1mm
Solovey [42]	2010	3D	Level set	No	CCA, ICA, ECA	2 (3D)	Seed points inside lumen
Gill [40]	2000	3D	Dynamic balloon model	No	CCA, ICA, ECA	1 (3D)	Initialization of balloon model inside lumen
Guerrero [41]	2007	2D	Star Kalman filters	No	CCA, ICA, ECA	3 (2D B-mode US sequence)	Seed points inside the lumen
Zahalka [39]	2001	2D	Active contours	No	CCA	2 (3D B-mode US sequence)	Seed points inside the lumen
Abolmae. [37]	2000	2D	Star algorithm and Kalman filtering	No	CCA	1 (2D B-mode US sequence)	Seed points inside the lumen
Mao [38]	2000	2D	Active contours	No	CCA	7 (B-mode)	Seed points inside the lumen

energy and a weak geometric prior in level set method. *Bhattacharyya* regional energy will be minimized when the probability distribution between foreground and background has maximum possible separation. Weak geometric prior influences the boundary to become convex which will not work in the presence of plaque. Lorza *et al.* [46] proposed a surface graph cuts based algorithm to segment the lumen with less user interaction but its performance was poor in patient images. Other algorithms [37–39] validated their algorithms for lumen segmentation on only seven 2D B-mode patient images [38], few phantom images [39], or did not provide quantitative segmentation validation [37].
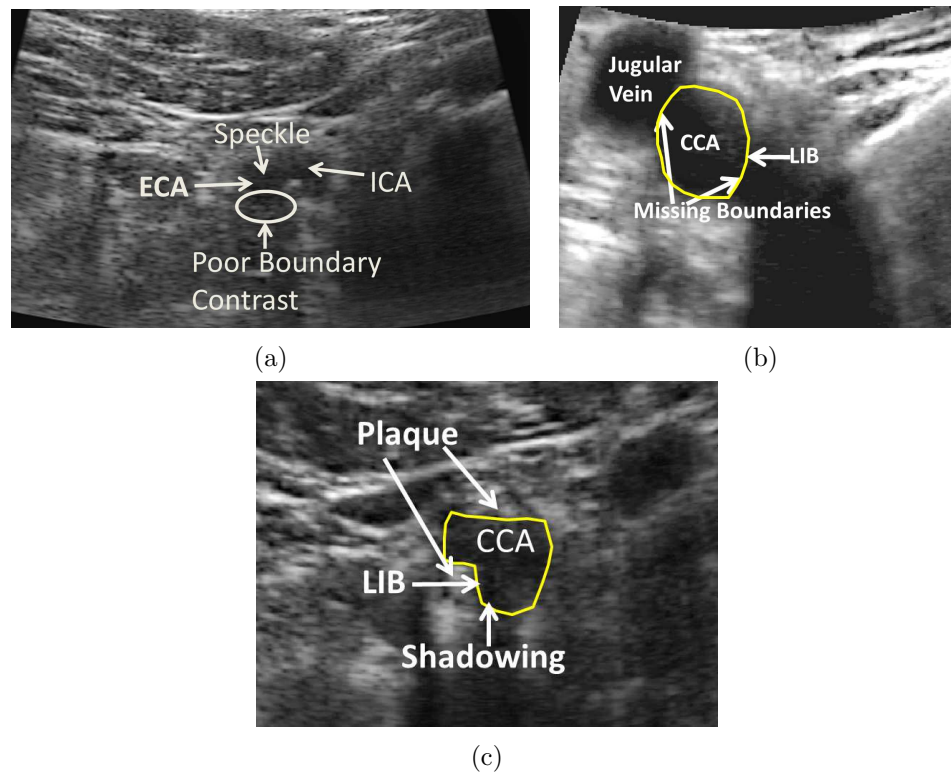
Figure 1.4: Challenges posed by US images a) Poor boundary contrast and speckle noise. b) Missing boundaries which are parallel to US beams. c) Shadow.

Yang *et al.* [44] proposed active shape model for the segmentation of both MAB and LIB of the common carotid artery. But, their algorithm requires a large number of training images to generate models and may be unable to segment complex plaque boundaries if complex plaques are not present in training images. Ukwatta *et al.* reported semiautomatic segmentation of MAB and LIB based on 2D [33] and 3D [45] level set method. Their algorithm can only segment the common carotid artery. But, the majority of plaques form at the carotid artery bifurcation and extend through the internal carotid artery (figure 1.5, figure 1.1). They progress along the vessel wall 2.4 times faster than they thicken [29].

Table 1.1 summarizes the main contributions and limitations of existing algorithms. To the best of our knowledge, there is no existing algorithms that can segment both LIB and MAB/AWB of CCA, ICA, and ECA.

1.4.2   Stopping Criteria

Due to the physics of ultrasound imaging, US images contain speckle noise (figure 1.4a), blurred boundary around anatomical regions (figure 1.4a), incomplete or missing tissue boundaries that are parallel to US beams (figure 1.4b), and shadowing (figure 1.4c). If these challenges are not addressed, there is a possibility of over segmentation due to leaking of an evolving contour through poor contrast boundary region.

A proper stopping criteria is needed to stop leaking of contour through poor contrast regions for an intensity based segmentation algorithm. Cohen *et al.* [47] used the norm distance between two curves at successive iterations and Leymarie *et al.* [48] developed change of potential field energy per unit length between two successive iterations for snake models as a stopping criteria. But Wong *et al.* [49] showed that both approaches suffer from wrong detection on image with no object, unable to locate small object and poor stability. The computational burden is very high for finding the corresponding points to calculate the norm distance for the level set method, which will eventually slow down curve evolution.

Yuan *et al.* [50] developed a dynamic stopping criteria based on given image property for mammography images. In their method, termination will be stopped when the weighted difference between mean slope of foreground (inside the contour) and background (outside the contour) converges to zero. But, we found that this stopping criterion did not show any converging trends for US image of the carotid artery. The intensity difference between background and foreground is high for breast lesion in mammographic images. If speckle noise is very high (figure 1.4a) for carotid images, the intensity difference between background and foreground becomes low, and this stopping criterion does not show any decreasing trend when an evolving contour reaches boundary.

Chaudhury *et al.* [51] proposed changes of contour length between successive iterations as a stopping criteria. We found that changes of contour length between successive iterations showed poor stability for US images of the carotid artery, whereas change of modified haussdorf distance (MHD)[52] between contours at successive iterations showed a decreasing
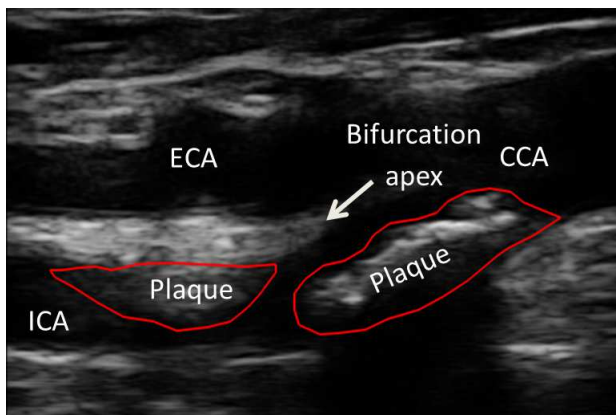
Figure 1.5: Plaque progresses through ICA.

trend [53]. Ukwatta *et. al.* [33] used change of the area bounded by contours at successive iterations as a stopping criteria for the level set method. It is better to use percentage change of area inside the evolving contour because the percentage change is insensitive to the size of the artery. But a single threshold based stopping criteria (like the change of area bounded by contours at successive iterations) will not be able to segment the right boundary at different locations: common, bifurcation, or internal carotid artery due to the challenges posed by US images (figure 1.4).

1.5 Research Objectives

3D US imaging of atherosclerotic carotid arteries poses several unique challenges (figure 1.4) for developing segmentation algorithms of LIB and AWB. These challenges should be addressed for developing a successful segmentation algorithm. One approach to overcome these difficulties is to supplement the information derived from the ultrasound image with prior knowledge about the object to be segmented which will bear close resemblance to how medical imaging data is interpreted by human experts in clinical practice.

3D segmentation of the carotid artery wall can be done in two ways: (i) application of 2D segmentation on cross-sectional slices and then render the segmented boundary from cross-sectional slices to generate a volume (ii) direct application of 3D segmentation algorithm. Though the 2D segmentation algorithm is computationally efficient, it does

not use out-of-plane information. Extension of some 2D segmentation algorithms to 3D algorithms are conceptually straightforward. However, the required computations for 3D segmentation on huge data is not computationally efficient.

Considering the challenges (figure 1.4) posed by 3D US images, the objectives of this research are as follows:

1. Develop semi-automatic 2D and 3D segmentation algorithms for segmenting LIB and AWB of the carotid artery from proximal CCA to distal ICA and ECA with the following characteristics:

   - Minimal user interaction and higher reproducibility.

   - Close resemblance of human interpretation of US images.

   - Efficient in terms of computational cost and memory storage.

2. Develop a novel stopping criteria to stop the leaking of contour through poor contrast regions (figure 1.4) and compare the performance of our stopping criteria with existing stopping criteria.

Chapter 2: Materials and Methods

The segmentation algorithm must be validated on US images of patients because it is not realistic to use phantom images to validate the accuracy of the algorithm as they do not simulate the characteristics of patient images. 3D US imaging was used to capture 3D images of atherosclerosis carotid artery. In this chapter, we will discuss about the study subjects, 3D US imaging system, and our proposed algorithm.

2.1   Materials

A sonix MDP Ultrasound system (Ultrasonix Medical Corporation, British Columbia, Canada) and a 4D L14-5/38 linear probe (figure 2.1a) were used to acquire 3D ultrasound images of carotid artery including the stenosis. The Stradwin software [1] was used for manually outlining the ultrasound volumes and the segmented isosurfaces were exported and further analyzed using MATLAB (Mathworks Inc, Natick MA). The proposed algorithm was implemented in MATLAB on a desktop with an Intel core 2 duo processor and 4 GB of RAM.

2.1.1   Study Subjects

Subjects were recruited at Veteran Affairs Medical Center, Baltimore, MD. All subjects had asymptomatic carotid stenosis and were diagnosed using Doppler US. Asymptomatic carotid stenosis patients do have previous symptoms of stroke or transient ischemic attack. All subjects provided written informed consent to the study procedures, which were approved by our Institutional Review Board. Color doppler images along with 3D US images of the carotid artery were acquired.

2.1.2 Image Acquisition and Post-processing

(a)   (b)
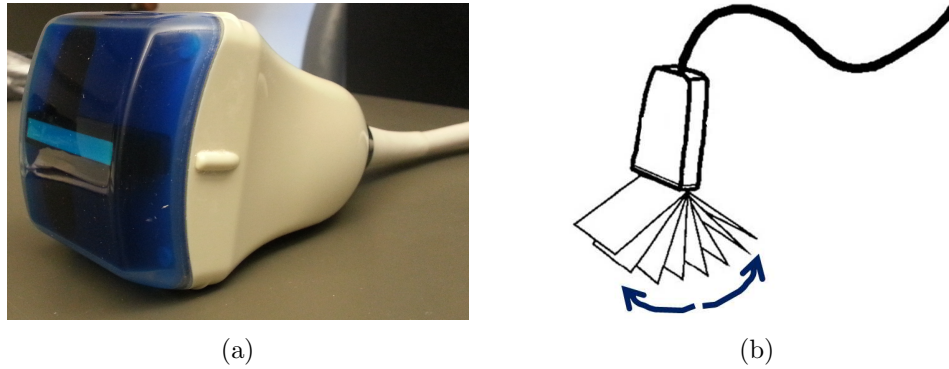
Figure 2.1: a) A 4D L14-5/38 linear probe by Ultrasonix Medical Corporation for acquiring 3d US image. b) A series of 2D images are collected as the transducer is tilted and then reconstructed into a 3D image in tilt scanning approach.

Sonix MDP is a diagnostic ultrasound system with a research interface. The device can perform all clinical functionalities in research mode. Image information can be retrieved for further processing. 4D probe is a mechanically augmented 1D ultrasound transducer array. 4D probe continuously acquire 2D B-mode images while the motorized drive mechanism is used to tilt the transducer about an axis parallel to the transducer face [54]. It forms a fan of images radial to the axis (figure 2.1b). The probe housing remains at a single location on the patients skin. Due to the fan-like geometry of acquired the 2D images, a large region of interest can be swept with an equal angular separation between 2D images. The angular separation between 2D images can be adjusted to yield high quality images. Due to the compactness of the 4D probe, it is very easy for hand-held positioning and manipulation. It can capture 3D volume within a heart cycle. The patient needs to remain motionless so that motion artifacts do not corrupt the image. The resolution of acquired 3D images are not isotropic. The linear distance between acquired image planes increases with distance due to the fan-like geometry, resulting in decreased spatial sampling and lower spatial resolution. Due to beam spreading in the scan direction, as well as within the acquired image plane, the resolution of pixels will degrade with distance from axis of rotation [54].

(a)   (b)   (c)
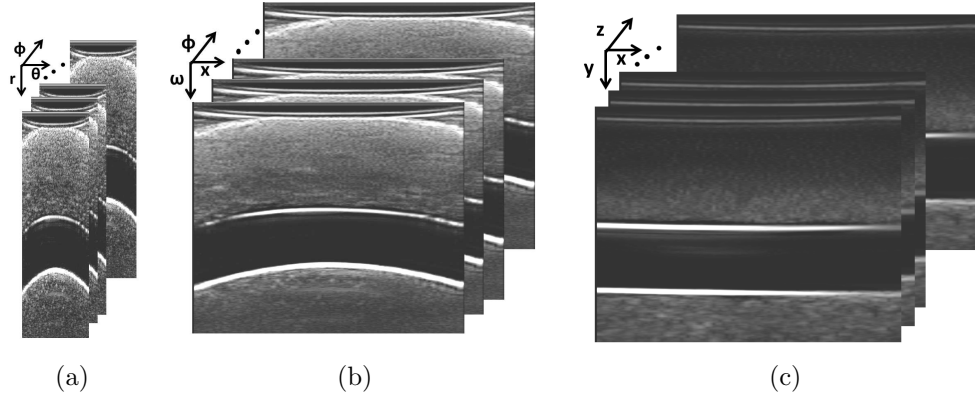
Figure 2.2: Process of separable 3D scan conversion (SC) in a phantom image of carotid artery. Separable 3D SC consists of two passes of 2D SC. a) Each $r - \theta$ image acquired in longitudinal plane and ϕ is the angle of this acquired longitudinal images in scan direction. b) An intermediate volume is generated from acquired volume in a) by first pass or axial-lateral SC. In axial-lateral SC, each $r - \theta$ image is converted to each $\omega - x$ image by interpolation. c) 2nd pass or axial-elevation SC is applied to convert data in $\omega - \phi$ of the intermediate volumes to data in $y - z$ plane of the final scan-converted volume.

In US imaging, axial (r in figure 2.2a) and lateral (θ in figure 2.2a) directions are defined as the direction parallel and perpendicular to the direction of US beam respectively. The swiveling direction is defined as elevation direction (ϕ in figure 2.2a) in 3D US imaging. The acquired 3D images consist of series of r-θ images (figure 2.2a). Each r-θ image consists of a group of polar coordinate vectors acquired in one longitudinal plane and ϕ is the angle of this acquired longitudinal images in scan or elevation direction. The acquired volume (figure 2.2a) is stored in memory. A separable 3D scan conversion (SC) [55] was applied in post-processing to generate the final scan-converted volume (figure 2.2c) in cartesian coordinate from input the volume in (figure 2.2a) because cartesian coordinates system gives better visualization of organs. It is also easier to develop a segmentation algorithm in the cartesian coordinate. A separable 3D SC is equivalent to performing a series of 2D SC on axial-lateral 2D images followed by a series of 2D SC on axial-elevation 2D images. It requires the generation of an intermediate volume (figure 2.2b). Each $\omega - x$ plane (figure 2.2b) in the intermediate volume is generated from each $r - \theta$ plane (figure 2.2a) through interpolation. This process is called first pass or axial-lateral SC. After axial-lateral SC, axial-elevation SC is applied to generate each $y - z$ plane in final volume (figure 2.2c)

15
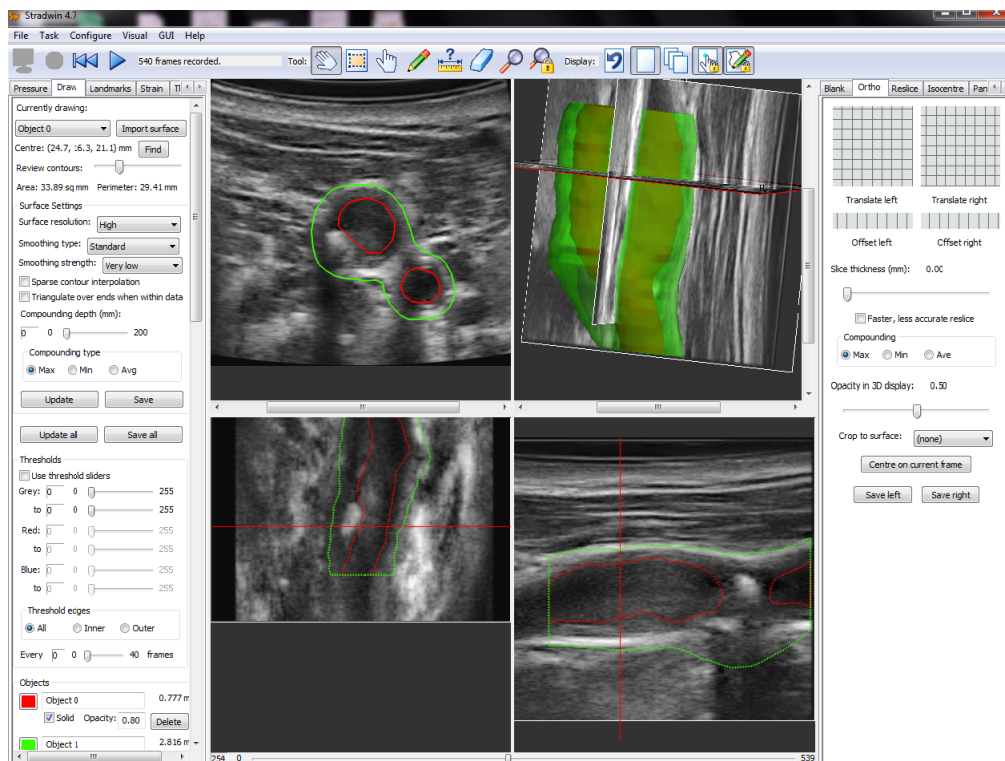
Figure 2.3: Stradwin interface for manual segmentation [1].

from each $\omega - \phi$ plane in the intermediate volume (figure 2.2b) through inverse mapping and interpolation.

After separable 3D SC, voxels in the 3D images become isotropic and the dimension of voxels ranges from 0.06 mm to 0.09 mm in our data set.

2.1.3   Manual Segmentation of Carotid Artery Wall

Due to the absence of ground truth boundaries, the proposed algorithm was compared against manual segmentation. Stradwin software (figure 2.3) [1] was used for manual segmentation. 21 cross sectional slices were selected from each 3D US patient image at an interslice distance of 1mm. We assume that the morphology of the carotid artery does not change a lot within 1mm. Observers delineated LIB and AWB in cross-sectional slices of the carotid artery, as seen in the top left window of stradwin (figure 2.3). The two bottom windows show the segmented boundary in the other two longitudinal slices.

16
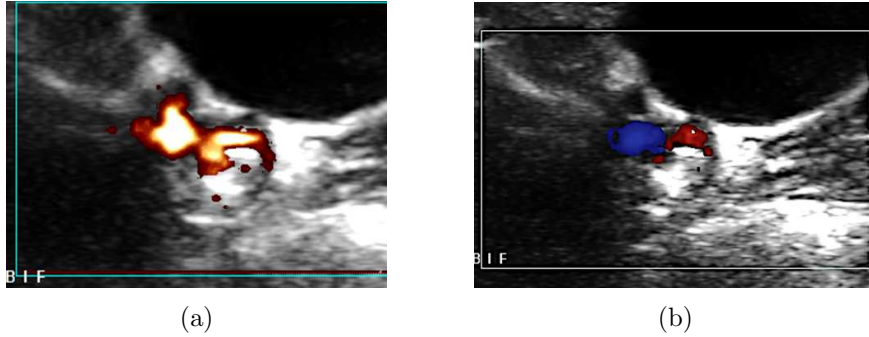
Figure 2.4: a) Power and b) color doppler images of carotid artery at the bifurcation region.

Observers can use the aid of the segmented boundary in longitudinal slices to modify the boundary in cross-sectional slices. The top right window shows the 3D surface generated from the segmented boundary. Stradwin automatically interpolates between boundaries to generate the surface. Observers took the aid of power (figure 2.4a) and color (figure 2.4b) doppler images for delineating LIB. US video of the carotid artery exam was also available to observers. Observers also looked at pulsation of arterial wall in the video for better identification of AWB. Viewing the video loop through systole and diastole will also give observers to get the best appreciation for the size of the lumen. When the boundary is missing in some portions of AWB or LIB, observers assumed that the boundary in that portion are in the same level as the nearest visible boundary.

2.2 Segmentation Algorithm

The assessment of carotid artery remodelling due to atherosclerosis directly from the 3D ultrasound volume is a difficult task due to the nature of ultrasound imaging. Quantitative assessment of the carotid artery remodelling can be done by segmenting artery wall. Image segmentation is the division of an image into number of non-overlapping regions. The boundary between regions is not known in advance. So the goal of the image segmentation task is to classify each image pixel as belonging to one of the regions such that few pixels are mis-classified. In case of the carotid vessel wall segmentation, the whole image can be divided into three regions: lumen, vessel wall including plaques, and remainder

17
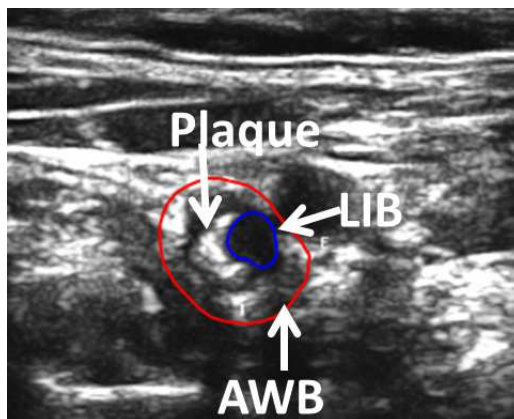
Figure 2.5: Division of image into three regions for performing image segmentation.

of image or background (figure 2.5). These three regions can be identified by outlining lumen-intima boundary (LIB) and adventitial wall boundary (AWB) of the carotid artery. Manual outlining of LIB and AWB is tedious, time consuming and suffers from intra- and inter-observer variability. Semi-automatic segmentation technique will reduce the time with higher reproducibility.

Image segmentation is a fundamental task in image analysis. Computer vision and medical image analysis community have developed a lot of algorithms for image segmentation. Algorithms developed for computer vision application are different from medical image analysis application. Most of the segmentation approaches are customized to the domain of its application. Due to inherent noisy and echogenic nature of US images, there is a need for significant adaption of any segmentation approach.

Table 2.1 summarizes our proposed segmentation algorithm which can be divided into four major parts: (i) initialization, (ii) image preprocessing, (iii) distance regularized level set evolution, and (iv) stopping criteria. In the first step, the user places points for LIB and AWB in only seven cross sectional slices and initialization on other slices is found by interpolation. The LIB and AWB are simultaneously segmented from the preprocessed image using distance regularized level set method [56] by optimizing an objective function consisting of smoothness energy, speed function, regularized energy, mean separation local (AWB)/ global (LIB) energy, ellipse fitting energy (2D algorithm for AWB), and stopping

18

Table 2.1: Block diagram describing the general work flow of the algorithm.

1. Initialization	2. Image Processing	3. Distance Regularized Level Set Method	4. Stopping Criteria
Manual: 1. Find bifurcation and selection of slices for initialization 2. Selection of boundary points **Automatic:** 1. Generation of initial points by interpolation 2. Generation of stopping boundary (2D) and surface (3D) 2. Generation of initial boundary (2D) and surface (3D)	**Lumen intima boundary:** 1. Local entropy based thresholding 2. Speckle reducing anisotropic diffusion **Adventitial wall boundary:** 1. Gaussian low pass filtering	**Energy Function for lumen intima boundary:** 1. Distance regularized energy 2. Length minimization energy 3. Area minimization energy 4. Mean separation local regional energy 5. Global uniform modeling regional energy 6. Stopping boundary (2D) or surface (3D) based energy **Energy Function for adventitial wall boundary:** 1. Distance regularized energy 2. Length minimization energy 3. Area minimization energy 4. Mean separation local regional energy 5. Ellipse fitting energy (2D) 6. Local smoothness energy (3D) 7. Stopping boundary (2D) or surface (3D) based energy	Change of modified hausdorff distance between contours at successive iterations

boundary (2D algorithm) or surface (3D algorithm) based energy functions. Our novel stopping criteria is a combination of stopping boundary based energy function and change of modified Haussdorf distance (MHD) [57] between contours at successive iterations for 2D segmentation algorithm. For 3D segmentation algorithm, we used combination of a stopping surface based energy and percentage change of pixel locations as stopping criteria. The narrowband implementation of the level set method helps us to use only one label function.

2.2.1 Initialization

First step of the algorithm is the initialization of points on the LIB and AWB. Then, stopping and initial boundaries are generated from these initial points.
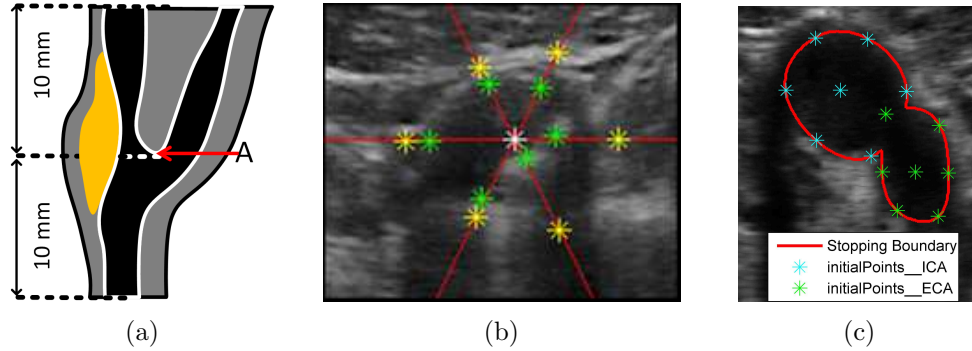
Figure 2.6: a) Bifurcation point in a carotid artery b) Selection of initial points. Legend: red=line at different angles,white=centroid of lumen, green=initial Points on LIB ,yellow=initial points on AWB c) Initialization at proximal slice of bulb. A final SB is found by taking union between two contours formed from initial points.

Find Bifurcation (BF) Point and Selection of Slices for Initialization.

The BF point (point A at figure 2.6a) was first located on sagittal slices and the corresponding cross-sectional slice was found. The common carotid artery was segmented proximally a distance of 10 mm from the bifurcation (BF) point and the internal and external carotid branches were each segmented distally a distance of 10 mm from the BF point. Then, 2D cross-sectional slices at an inter-slice distance of 1mm were selected. Cross-sectional slices for manual initialization of points were selected at an inter-slice distance of 4mm. So, 7 (including BF slice) out of 21 cross-sectional slices were selected for manual initialization of points. Initialization of other slices was generated by interpolation. Same initial points were used for 2D and 3D segmentation algorithm.

Selection of Boundary Points.

A boundary based initialization was used by placing initial points on the LIB and AWB. Initial boundary (2D algorithm) or surface (3D algorithm) for level set evolution and stopping boundary (2D algorithm) or surface (3D algorithm) were generated from these initial points. For each boundary, observer places six points on the image. First, the observer places the first point in centroid of lumen and straight lines were drawn automatically passing through the centroid point with angles: 0^0, 60^0 and 120^0 (figure 2.6b). Then, the

| (a) | (b) |
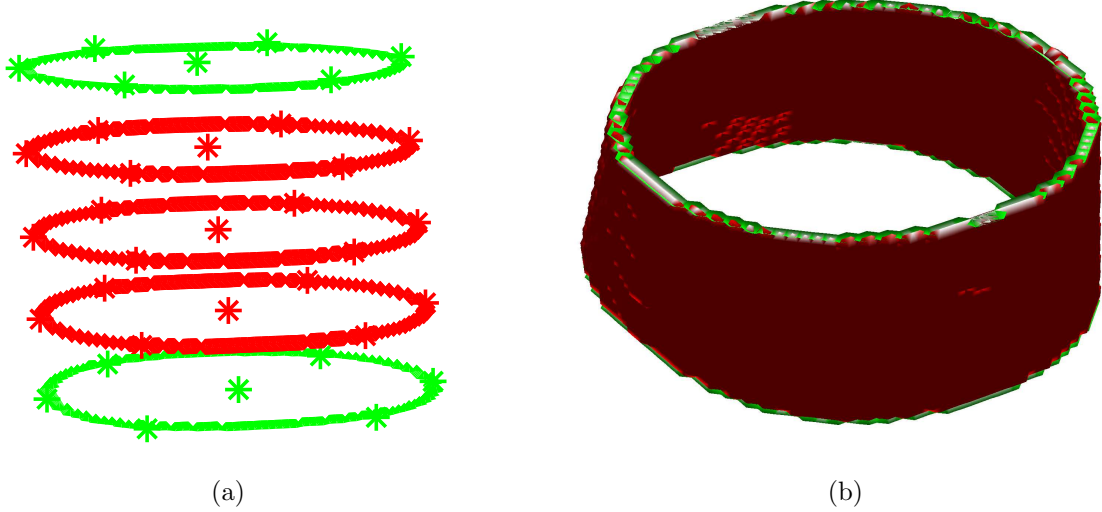
Figure 2.7: a) Interpolated initial points (red *) with manual initial points (green *) for 2D segmentation algorithm. Stopping boundary (ellipse in this case) is generated by spline interpolation through these initial points. The distance between cross-sectional slices for manual initialization was 4mm. But, the distance between each cross-sectional slices was 1mm. b) Manually initial points (green *) with interpolated initial points (red *) for 3D segmentation algorithm. The distance between each cross-sectional slices is 0.067mm that is the pixel dimension in the z-direction.

user chooses initial points at the intersection of these lines with AWB and LIB boundary (figure 2.6b). The fixed angles in initialization reduces user variability in initialization and are used as landmarks for interpolation. Initialization was done separately for ICA and ECA at bulb region and after the BF (figure 2.6c). The initialization on the other cross sectional slices were found by doing interpolation. Figure 2.7 shows interpolated initial points (red *) with manual initial points (green *) for 2D segmentation. The proposed 2D segmentation algorithm was applied on each cross-sectional slices. The inter-slice distance between cross-sectional slices was 1mm for 2D segmentation. The input to the proposed 3D segmentation algorithm was a 3D mesh. The pixel dimension in z-direction was 0.06 -0.09mm i.e., the distance between each cross-sectional slices was 0.06-0.09mm. All cross-sectional slices were used for 3D segmentation.
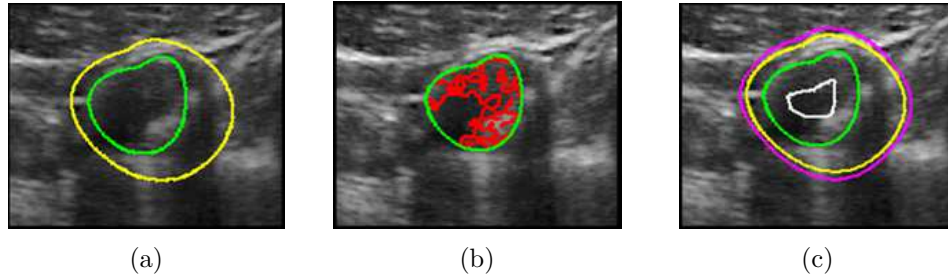
Figure 2.8: a) Stopping boundary from initial points (green:LIB, yellow:AWB). b) Edge map (red) inside SB (green). c) Initial boundary for LIB (white) and AWB(purple).

Generation of Stopping Boundary (2D) and Stopping Surface (3D).

A stopping boundary (SB) was generated by 2D cubic spline interpolation through initial points (figure 2.8a). At bulb region and after the BF region, SB is the union between two contours formed from initial points (figure 2.6c). Initial points were selected in such a way that SB went through the correct boundary at shadowing or poor boundary contrast regions. There will be no problem even if SB goes through a wrong boundary in the plaque (figure 2.8a) or high contrast region because the evolving contour will stop at high contrast boundaries due to an edge gradient. Figure 2.7 shows the generated SB from manual and interpolated initial points where manually initialized cross-sectional slices were 4mm apart. Manual initialization was done on seven cross-sectional slices for a single 3D US image and generated SBs from these initialization are shown in figure 2.9a. SB in other cross sectional slices generated from interpolated initial points is shown in figure 2.9b. The distance between each SB in figure 2.9b is 1mm. A triangular surface (figure 2.9a) was also generated from interpolated initial points for 3D segmentation algorithm.

Generation of Initial Boundary (2D) and Initial Surface (3D).

SB was dilated to serve as initial boundary (IB) for AWB contour evolution (figure 2.8c). A 'disk' shaped mask was used for dilation. Due to the smoothness of AWB, the radius of the disk was 3 for dilation (purple contour is dilated from yellow contour in figure 2.8c). IB for LIB contour evolution was generated by eroding the SB of LIB (white contour is eroded
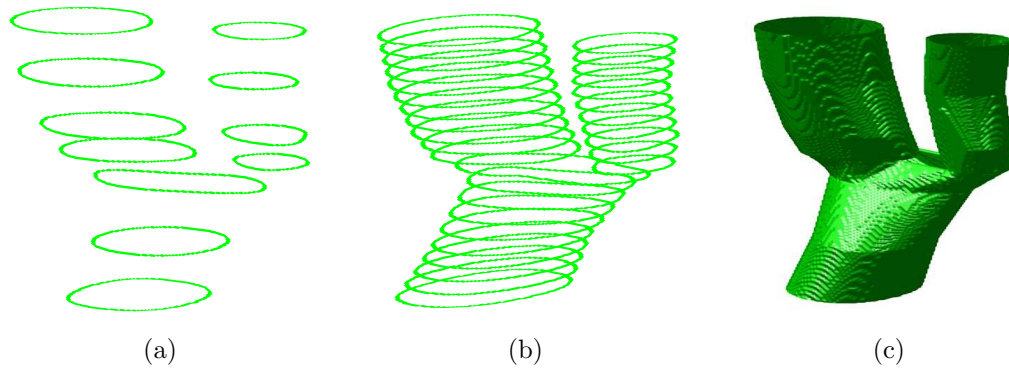
Figure 2.9: a) Stopping boundary in 3D generated from manual initialization. b) Stopping boundary in 3D generated from manual initialization and interpolation for 2D segmentation algorithm. c) Stopping surface for direct 3D segmentation.

from green contour in figure 2.8c). As plaque grows inside lumen, a fixed radius mask can not be used. The radius of the 'disk' shaped mask for LIB is found automatically from the image characteristics. The steps for finding the radius are as follows :

1. A binary mask was created from SB by making all pixels inside SB to 1.

2. A canny edge detector was applied to find the edge map image of original 2D cross-sectional image.

3. The binary mask was multiplied by the edge map image to find the edge map inside SB (figure 2.8b).

4. Distance to SB (white asterisk in figure 2.6b) from each point on the edge Map (figure 2.8b) was calculated and point

5. The point on edge map which is at the largest distance was found.

6. The largest distance is the radius of the 'disk' shaped mask.

Figure 2.8c shows the IB for LIB and AWB. Figure 2.10a shows IB generated from manual initialization of the SB. IB for each cross-sectional slices at an ISD of 1mm was generated from corresponding SB for 2D segmentation algorithm (figure 2.10b). A triangular surface (figure 2.10c) was also generated for 3D segmentation algorithm.
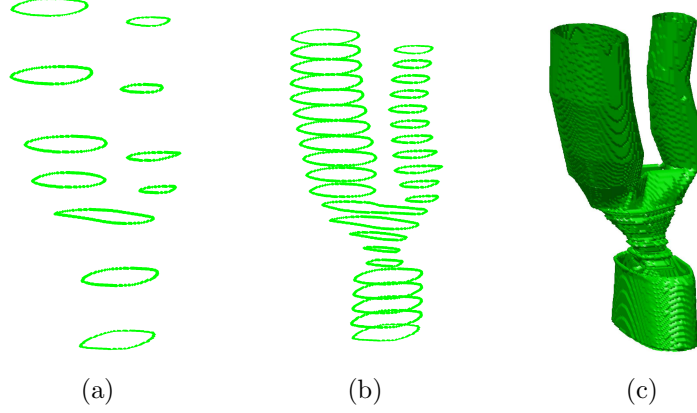
Figure 2.10: a) Initial Boundary in 3D generated automatically from manually initialized SB. b) Initial Boundary in 3D for 2D segmentation algorithm . c) Initial surface for direct 3D segmentation.

2.2.2 Image Preprocessing

Though, the human eye is able to derive the meaningful information from US images, automatic processing is very difficult in US images due to its speckle noise and artifacts. A low pass Gaussian filter was applied to smooth out image for AWB segmentation. For a d-dimensional image $U(\mathbf{x})$, Gaussian filter was defined as

$$\overline{U}(\mathbf{x}) = \sum_{\mathbf{y} \in N(\mathbf{x})} G_\sigma(\mathbf{x} - \mathbf{y}).U(\mathbf{y}) \qquad (2.1)$$

where $G_\sigma(\cdot)$ is a Gaussian kernel and standard deviation σ controls degree of smoothing.

$$G_\sigma(x) = \frac{1}{(2\pi\sigma^2)^{d/2}} exp\left(-\frac{|x|^2}{2\sigma^2}\right) \qquad (2.2)$$

A combination of local entropy based thresholding [58] and speckle reducing anisotropic diffusion (SRAD) [59] filtering was used to pre-process the 2D cross-sectional images for LIB Segmentation.

The application of entropy filtering was optional and it was applied only if there was a

strong image artifact in the lumen. Entropy is invariant to gray level transformation. We found empirically that 4-connected pixels in the lumen had entropy of 3.5-4. Our entropy threshold value was 4. Pixels whose 4-connected neighborhoods had local entropy less than the threshold are set to one.

SRAD is an anisotropic diffusion process and it smoothes homogeneous regions of ultrasound speckle while preserving image edges. Anisotropic diffusion process creates a scale space by generating more and more blurred images. It is implemented by means of an approximation of the generalized diffusion equation where each new image is computed by applying a diffusion equation to the previous image. So it is an iterative process that occurs over time.

For a given intensity image $U(x, y)$, the SRAD process generates a sequence of solutions $U(x, y; t)$ to the partial differential equations

$$\frac{\delta U(x, y; t)}{\delta t} = div[c(q) \nabla U(x, y; t)] \tag{2.3}$$

where t symbolizes time since initialization, div is the divergence operator, ∇ is the gradient operator, and $c(q)$ is the image-dependent diffusion coefficient.

The diffusion process is initialized by the original image U_0 :

$$U(x, y; 0) = U_0 \tag{2.4}$$

The image-dependent diffusion coefficient [60] $c(q)$ is defined as

$$c(q) = \left[1 + \frac{[q(x, y; t)^2 - q_0^2(t)]}{q_0^2(t)[1 + q_0^2(t)]} \right]^{-1} \tag{2.5}$$

where $q(x, y; t)$ is the instantaneous coefficient of variation and $q_0(t)$ is the coefficient of variation in a homogeneous region with well developed speckle.

$q(x, y; t)$ works as an adaptive speckle-detecting function. It depends on the instantaneous

25

Figure 2.11: a) Before SRAD b) After SRAD. SRAD enhances the boundary.

coefficient of variation to perform edge detection in a speckle contaminated image. $q(x, y; t)$ is defined as [60]

$$q(x, y; t) = \sqrt{\frac{\left| \frac{1}{2} \left(\frac{|\nabla_\sigma U|}{U} \right)^2 - \frac{1}{16} \left(\frac{\Delta U}{U} \right)^2 \right|}{\left[U + \frac{1}{4} \frac{|\nabla_\sigma U|}{U} \right]}} \tag{2.6}$$

$q(x, y; t)$ in equation 2.6 combines a normalized gradient magnitude $|\nabla_\sigma U|$ and a normalized Laplacian operator ΔU to perform edge detection. This edge detector adapts to the variations in average intensity due to normalization. Due to this normalization, speckle will be detected in both dark and bright regions. High relative gradient magnitude and low relative laplacian indicates an edge.

A speckle scale function, $q_0(t)$, indicates the average speckle dimensions and it can be calculated as a function of mean and variance over a homogenous region of image U [59] or be defined by [61]

$$q_0(t) = \frac{\lambda \int_\Omega q^2(x, y; t) dx}{\int_\Omega dx} \tag{2.7}$$

where λ control the scale selection for preserving edge and Ω represents image domain. Figure 2.11 shows the application of SRAD on 2D cross-sectional images. SRAD enhances the boundary.

2.2.3 Distance Regularized Level Set Evolution

The level set method, introduced by Osher and Sethian [62], is an iterative energy minimization framework to find a possible decision boundary (contour) C for dividing an image domain Ω into sub-domains Ω_A and Ω_B. The decision boundary is a geometrical object which is a curve in 2D or a surface in 3D. Energy minimization is an optimization problem and the smallest energy of C will give the final segmentation.

Level set method can capture dynamic interface and complex shapes without parameterizing the segmentation curve. It is also able to handle topological changes such as splitting and merging automatically. Numerical computation of the level set method can be implemented on a fixed Cartesian grid due to its non-parametric representation of the decision boundary. The level set method has been widely used for the segmentation of ultrasound images [63].

In the level set method, a contour or hyper-surface of interest is embedded as zero level set of higher dimensional function, called level set function (LSF). Let $\phi(\mathbf{x}) : \Omega \rightarrow \Re$ represents a LSF in an image domain Ω. $\mathbf{x} \in \Omega$ is a spatial variable representing a pixel in Ω domain i.e. $\mathbf{x} = (x, y)$ and $\mathbf{x} = (x, y, z)$ for 2D and 3D images respectively. $\phi(\mathbf{x})$ separates the image domain Ω into inside (Ω_A) and outside (Ω_B) sub-domains. $\phi(\mathbf{x})$ has following properties

$$\phi(\mathbf{x}) > 0 \quad \text{for} \quad \mathbf{x} \in \Omega_A$$

$$\phi(\mathbf{x}) < 0 \quad \text{for} \quad \mathbf{x} \in \Omega_B \tag{2.8}$$

$$\phi(\mathbf{x}) = 0 \quad \text{for} \quad \mathbf{x} \in \partial\Omega = \Gamma$$

The *zeroth level* of $\phi(\mathbf{x})$ represents the decision boundary $\partial\Omega = \Gamma$ (i.e. spatial variables $\mathbf{x}$ for which $\phi(\mathbf{x}) = 0$ represents points on the boundary). Figure 2.12 shows an implicit representation of the decision boundary Γ in level step method. During the segmentation process, $\phi(\mathbf{x})$ will evolve, which will cause an evolution of points in the boundary $\mathbf{x}$ and the decision boundary Γ will follow the topology automatically. Figure 2.12 shows that Γ curve underwent topological changes by merging into one.

27
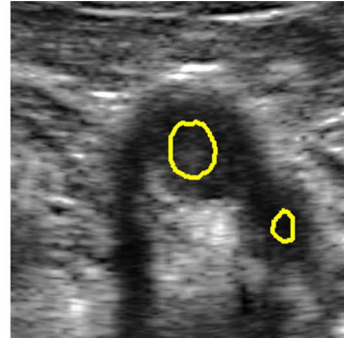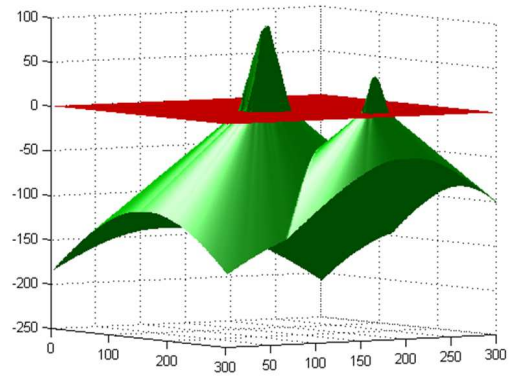
(a) t=0
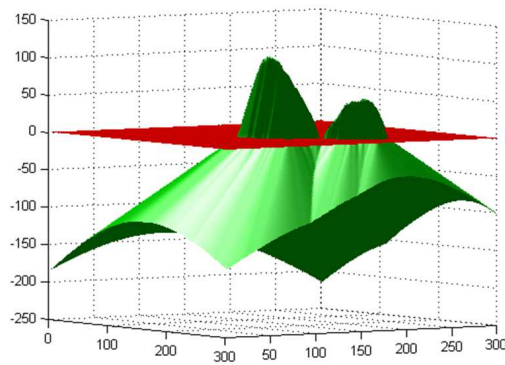
(b) t=10
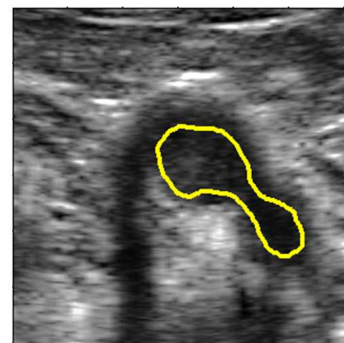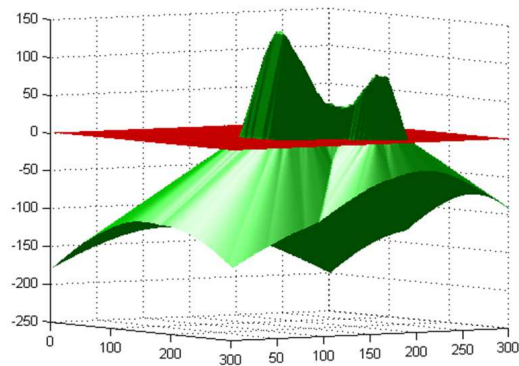
(c) t=20

Figure 2.12: Implicit representation of decision boundary in level set method. left column: Evolution of level set function $\phi(\mathbf{x})$ (green) in time with its zeroth level cross-sectional slice (red). right column: Zeroth level cross section of $\phi(\mathbf{x})$ in time.

In level set method, the decision boundary evolution is defined as [64]

$$\frac{\partial \phi(\mathbf{x})}{\partial t} = -\frac{\partial \xi}{\partial \phi(\mathbf{x})} |\nabla \phi(\mathbf{x})| = F|\nabla \phi(\mathbf{x})| \tag{2.9}$$

which is known as a level set evolution equation. In equation 2.9, $\frac{\partial \xi}{\partial \phi(\mathbf{x})}$ is first variation of energy functional ξ, ∇ is a gradient operator, and F is the speed function that controls the motion of the contour with respect to the artificial parameter t. The LSF $\phi(\mathbf{x})$ is generally defined as a signed distance function in terms of an initial contour C that divides the image domain Ω into Ω_A and Ω_B. $\phi(\mathbf{x})$ is defined as [64]

$$\phi(\mathbf{x}) = \begin{cases} d(\mathbf{x}, C), & \mathbf{x} \in \Omega_A \\ -d(\mathbf{x}, C), & \mathbf{x} \in \Omega_B \end{cases} \tag{2.10}$$

where $d(\mathbf{x}, C)$ is the minimum distance between $\mathbf{x}$ and the contour C. $\phi(\mathbf{x})$ has the following two properties

$$|\nabla \phi(\mathbf{x})| = 1,$$

$$\phi(\mathbf{y}) = 0, \quad \mathbf{y} \in \partial \Omega \tag{2.11}$$

LSF grows irregularities during its evolution in the conventional level set methods [62]. It causes numerical errors and eventually makes the level set evolution unstable. One of the solutions of this problem is reinitialization [64] of LSF to restore regularity of the LSF and maintain stable level set evolution. Reinitialization is performed periodically by stopping level set evolution and reshaping LSF as a signed distance function. Though reinitialization has been widely used in level set method , it may incorrectly move the zeroth level away from the expected position of the boundary[64, 65].

Due to the limitations of reinitialization in the conventional level set method, distance
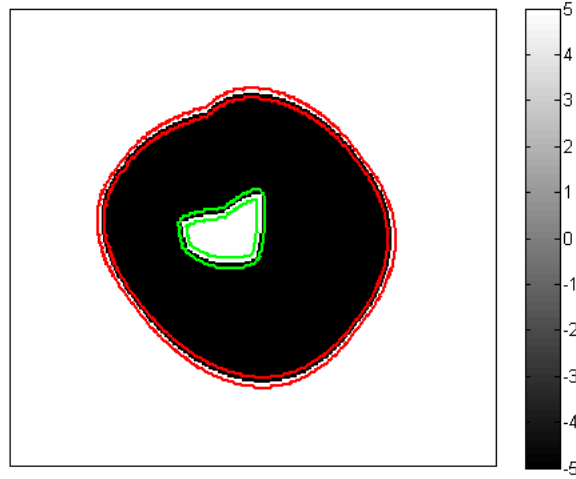
Figure 2.13: Initial Phi generated from initial LIB and AWB boundary. The red and green boundaries show the narrowband of LSF $\phi(\mathbf{x})$. The narrowband consists of zeroth level (white to black or black to white transition boundary) and 3×3 neighborhoods of zeroth level.

regularized level set evolution (DRLSE) [56] was used for the segmentation of AWB and LIB in this work. The advantage of DRLSE over conventional level set [62] method is that DRLSE doesn't require reinitialization to maintain stability and regularity.

In DRLSE, the initial level set function is defined as a binary step function i.e., sub-domain Ω_A and Ω_B initialized with constant positive and negative values. We used following initialization to segment the AWB and LIB simultaneously.

$$\phi_0(\mathbf{x}) = \begin{cases} -c_0, & \text{if } \mathbf{x} \in R_0 \\ c_0, & \text{otherwise} \end{cases} \tag{2.12}$$

where $c_0 > 0$ is a constant and R_0 is a region in the domain Ω enclosed by LIB (white boundary in figure 2.8c) and AWB (purple boundary in figure 2.8c) extracted at algorithm's initialization step. Figure. 2.13 shows the initial $\phi(\mathbf{x})$ for segmenting LIB and AWB simultaneously. It was generated using initial LIB and AWB boundary (figure 2.8).

30

Narrowband implementation of DRLSE, where the LSF is updated only around the neighbourhood of zeroth level , was used to reduce the computational cost. The narrowband consists of zeroth level (white to black or black to white transition boundary) and 3×3 neighborhoods of zeroth level. Figure 2.13 shows the narrowband around LIB (green) and AWB (red). Though LSF contains two step functions, there will be one step function in the narrowband of each boundary. So the implementation of energy functions will be the same in the narrowband of each boundary. It is very memory efficient because our implementation requires only one LSF. Though LIB and AWB contours are propagating simultaneously, there will be no intersection between them due to our the proposed stopping criterion. The level set evolution equation in DRLSE [56] is given by

$$\frac{\partial \phi(\mathbf{x})}{\partial t} = -\mu \frac{\partial R_p(\phi(\mathbf{x}))}{\partial t} - \frac{\partial \xi_{ext}(\phi(\mathbf{x}))}{\partial t} \tag{2.13}$$

where $R_p(\phi(\mathbf{x}))$ is the distance regularized energy [56] and $\xi_{ext}(\phi(\mathbf{x}))$ is the external energy functional that depends on the properties of the image.

Distance Regularized Energy.

The purpose of distance regularized energy [56] is to maintain the signed distance property $|\nabla \phi(\mathbf{x})| = 1$ only in the vicinity of the zeroth level while keeping $|\nabla \phi(\mathbf{x})| = 0$ at locations far away from the zeroth level. There is no need to reinitialize LSF to maintain regularity and stability due to this energy function. The level set regularized energy function [56] is defined by

$$R_p(\phi(\mathbf{x})) = \int_\Omega p(|\nabla \phi(\mathbf{x})|) \, d\mathbf{x} \tag{2.14}$$

where $p(\cdot)$ is a double well potential function that has minimum points at 1 and 0 to maintain the signed distance property $|\nabla \phi(\mathbf{x})| = 1$ in the vicinity of zeroth level and $|\nabla \phi(\mathbf{x})|$

= 0 at a location far away from the zeroth level.

The double well potential function $p(\cdot)$ [56] is defined as

$$p(s) = \begin{cases} \frac{1}{(2\pi)^2}(1 - \cos(2\pi s)), & \text{if s} \leq 1 \\ \frac{1}{2}(s-1)^2, & \text{if s} \geq 1 \end{cases} \qquad (2.15)$$

External energy is the combination of edge based energy, region based energy, and high level domain knowledge. The edge-based energy forces the contour to move towards the region of strong image gradient; whereas regional energy moves the contour without presence of image gradient; and domain knowledge based energy influences the contour to follow the expected shape of artery. The external energy functions used for AWB were different from LIB due to the image characteristics of LIB and AWB. The AWB has an elliptical shape (except at bifurcation). Some parts of AWB has high image gradient which are orthogonal to ultrasound beam but elsewhere has very poor image contrast. The shape of LIB is not fixed due to presence of plaque. Most part of LIB has high image gradient because the lumen region is very homogeneous. The external energy used for LIB and AWB is defined as

$$\xi_{ext}^{LIB} = \lambda_{LIB}\xi_L + \alpha_{LIB}\xi_A + \gamma_{LIB}\xi_{LR} + \nu_{LIB}\xi_{GR} + \beta_{LIB}\xi_{SB} \qquad (2.16)$$

$$\xi_{ext}^{AWB} = \lambda_{AWB}\xi_L + \alpha_{AWB}\xi_A + \gamma_{AWB}\xi_{LR} + \beta_{AWB}\xi_{SB} + \sigma_{AWB}\xi_E \quad \text{for 2D algorithm} \quad (2.17)$$

or

$$\xi_{ext}^{AWB} = \lambda_{AWB}\xi_L + \alpha_{AWB}\xi_A + \gamma_{AWB}\xi_{LR} + \beta_{AWB}\xi_{SB} + \rho_{AWB}\xi_{LS} \quad \text{for 3D algorithm} \quad (2.18)$$

where ξ_L, ξ_A, ξ_{LR}, ξ_{GR}, ξ_E,ξ_{LS}, and ξ_{SB} are the length minimization energy, area minimization energy, local mean separation regional energy, global uniform modeling regional

<center>(a)   (b)</center>
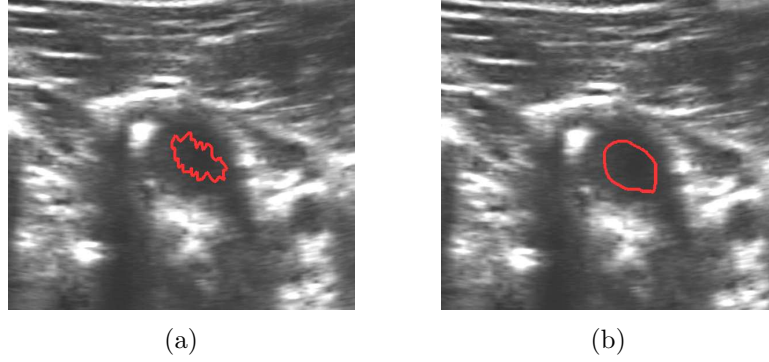
Figure 2.14: a) Without length minimization energy b) With length minimization energy.

energy , ellipse fitting based energy, local smoothness energy, and stopping boundary based energy respectively. $\lambda_{LIB/AWB}$, $\alpha_{LIB/AWB}$, $\gamma_{LIB/AWB}$, $\beta_{AWB/LIB}$, σ_{AWB}, ρ_{AWB}, and ν_{LIB} are weight of the corresponding energy functions.

Length Minimization Energy (ξ_L).

ξ_L [56] smooths the contour by minimizing the arc length of the contour (figure 2.14). As it is weighted by edge detector function g, it will be minimized at the boundary. It is defined by

$$\xi_L = \int_\Omega g\delta(\phi(\mathbf{x})) \ d\mathbf{x} \tag{2.19}$$

where $\delta(\mathbf{x})$ is dirac delta function [64]. Edge detector function g [56] is defined as

$$g \triangleq \frac{1}{1 + |\nabla G_\sigma * I|^2} \tag{2.20}$$

where ∇G_σ is a Gaussian kernel with a standard deviation σ and I is image in the domain Ω. g is inversely proportional to the square of image gradient. Numerically, $\delta(\mathbf{x})$ is calculated as

$$\delta(\mathbf{x}) = \begin{cases} \frac{1}{2\in}[1 + cos(\frac{\pi \mathbf{x}}{\in})], & |\mathbf{x}| \leq \in \\ 0, & |\mathbf{x}| > \in \end{cases} \tag{2.21}$$

<center>33</center>

(a)   (b)
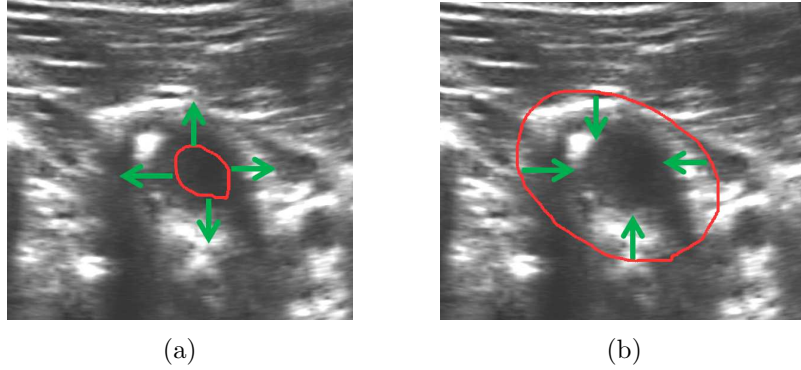
Figure 2.15: Arrow indicates the direction of propagation of contour for a) LIB b) AWB segmentation to minimize foreground area.

Area Minimization Energy (ξ_A).

ξ_A [56] speeds up the evolution of the contour by minimizing the area weighted by the edge detector function. It will minimize foreground area. Inside of AWB and outside of LIB are defined as foreground (figure 2.15). ξ_A will be minimum at the boundary due to edge detector function. It is defined as

$$\xi_A = \int_{\Omega} gH(-\phi(\mathbf{x})) \ d\mathbf{x} \tag{2.22}$$

where $H(\mathbf{x})$ is the regularized heaviside function [64] and is defined as

$$H(\mathbf{x}) = \begin{cases} \frac{1}{2\in}[1 + \frac{\mathbf{x}}{\in} + \frac{1}{\pi}sin(\frac{\pi\mathbf{x}}{\in})], & |\mathbf{x}| \leq \in \\ 1, & |\mathbf{x}| > \in \\ 0, & |\mathbf{x}| < -\in \end{cases} \tag{2.23}$$

Mean Separation Local Regional Energy (ξ_{LR}).

ξ_{LR} [66] will be minimized when the local interior and exterior (figure 2.16) regional means have the largest difference. The local region is formed within a radius r from each point on the boundary (figure 2.16). Let, $\mathbf{x}_l$ be an another spatial variable independent of $\mathbf{x}$ and

34
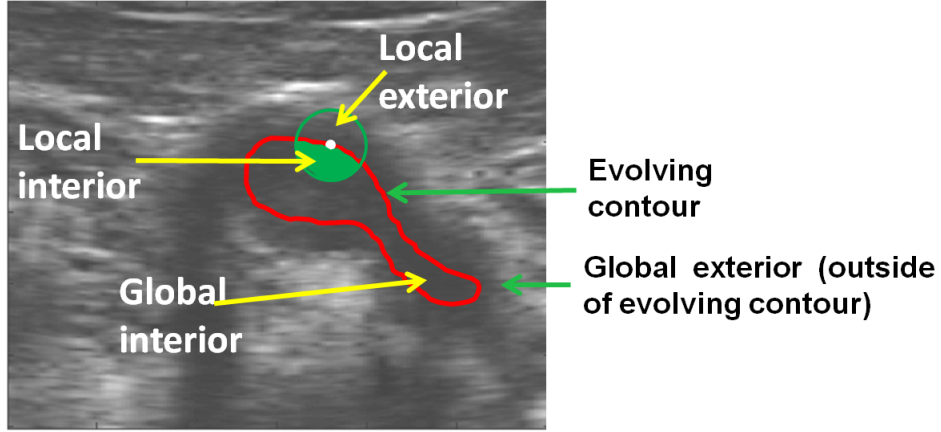
Figure 2.16: Local interior, local exterior, global interior, and global exterior region for the calculation of regional energy.

ξ_{LR} is defined by

$$\xi_{LR} = -\int_{\Omega_x} \delta\phi(\mathbf{x}) \int_{\Omega_{\mathbf{x}_l}} B_{LR}(\mathbf{x}, \mathbf{x}_l)(u_x - v_x)^2 \, d\mathbf{x} \, d\mathbf{x}_l \tag{2.24}$$

where $B_{LR}(\mathbf{x}, \mathbf{x}_l)$ is the localized circular shaped region of radius r and is defined as [66]

$$B_{LR}(\mathbf{x}, \mathbf{x}_l) = \begin{cases} 1, & ||\mathbf{x} - \mathbf{x}_l|| < r \\ 0, & \text{otherwise} \end{cases} \tag{2.25}$$

u_x and v_x are the interior and exterior mean intensities calculated on each point on the contour defined by the region r. If the value of r is large enough, B_{LR} will converge to global statistics but it will act as an edge detector for very small r.

Global Uniform Modeling Regional Energy (ξ_{GR}).

ξ_{GR} [67] is proposed by Chan *et al.* where the foreground and background are modeled as constant intensities represented by their means u and v. This energy will be minimized when the foreground and background are best approximated by their means. Usually, global
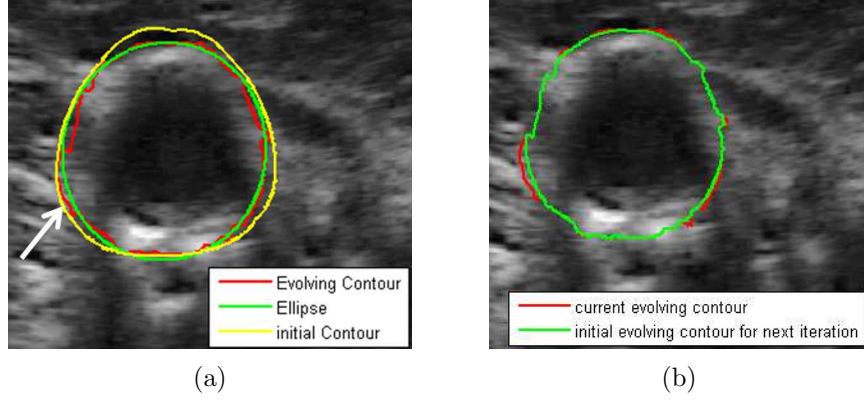
Figure 2.17: (a) Evolving contour at 60th iteration. It is stopped at local edge (marked by white arrow). Any parts of the evolving contour outside the fitted ellipse (green contour) will removed. (b) Initial evolving contour for 61th iteration after applying ellipse fitted energy.

regional energy is calculated on whole image (figure 2.16). A bounding box was calculated from stopping boundary of LIB. Twice size of bounding box was used to calculate ξ_{GR} instead of whole image in our proposed algorithm.

$$\xi_{GR} = \int_{\Omega} H(-\phi(\mathbf{x}))(I(\mathbf{x}) - u)^2 + (1 - H(-\phi(\mathbf{x})))$$

$$(I(\mathbf{x}) - v)^2 \, d\mathbf{x} \tag{2.26}$$

Ellipse Fitting Based Energy (ξ_E).

The initial contour for AWB was generated by dilating the stopping boundary using a fixed radius mask. There is a possibility that the evolving contour may be stalled at a local edge. As the speed of evolution of contour mainly depends on the edge, there will be no evolution of contour at regions without contrast difference. Even local regional energy may not be able to evolve contour at that region. We defined a novel ellipse fitting based energy ξ_E to overcome these problems. Ellipse fitting energy was defined for only 2D algorithm. In our energy calculation, first an ellipse was fitted through the evolving contour at each iteration (green contour in figure 2.17a). Then, a binary mask $\phi_{ef}(\mathbf{x})$ having negative value inside

36

the ellipse and positive value outside the ellipse was generated. The ξ_E will be minimized by removing any parts of evolving contour which are outside of $\phi_{ef}(\mathbf{x})$. Any parts of the evolving contour (red contour in figure 2.17a) outside the fitted ellipse (green contour in figure 2.17a) will be removed. Figure 2.17b shows the initial contour (green contour) for next iteration. The proposed ellipse fitting based energy is defined as

$$\xi_E = \int_\Omega \delta(\phi(\mathbf{x})) B_{ef}(\mathbf{x}) \ d\mathbf{x} \tag{2.27}$$

where

$$B_{ef}(\mathbf{x}) = \begin{cases} 1, & \phi_{ef}(\mathbf{x}) > 0 \\ 0, & \text{otherwise} \end{cases} \tag{2.28}$$

Local Smoothness Energy (ξ_{LS}).

As plaque grows inside lumen, the AWB has a generally smooth low-order shape. But, the segmented AWB may contain convex or concave regions due to the heterogeneity of image intensity of the interior and exterior of AWB. Therefore, segmentation algorithm based on solely edge-based or region-based energy may not yield an accurate segmentations. Local smoothness energy (ξ_{LS}) [68] was used in our proposed 3D segmentation algorithm to reduce the convexity and concavity of a local neighborhood region defined by a prolate spheroid mask. Let, $\mathbf{x}_{ls}$ be an another spatial variable independent of $\mathbf{x}$ and ξ_{LS} is defined by [68]

$$\xi_{LS} = \int_\Omega \delta\phi(\mathbf{x})(A_v(\mathbf{x}) - A_u(\mathbf{x}))^2 d\mathbf{x}, \tag{2.29}$$

where A_u and A_v are the volumes of the local interior and exterior regions defined by prolate spheroid mask $B_{LS}(\mathbf{x}, \mathbf{x}_{ls})$.

$$A_u = \int_{\Omega_{\mathbf{x}_{ls}}} B_{LS}(\mathbf{x}, \mathbf{x}_{ls}) H(\phi(\mathbf{x}_{ls})) \ d\mathbf{x}_{ls} \tag{2.30}$$

(a)   (b)
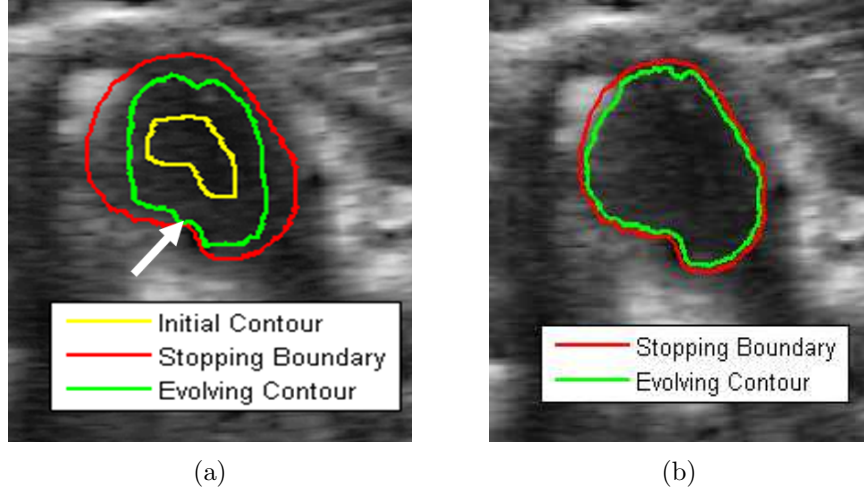
Figure 2.18: (a) Evolving contour at 100th iteration. There will be no movement (region marked by white arrow)of evolving contour(green contour) when it touches the stopping boundary (red contour) but evolving contour can propagate other direction. (b) Final evolving contour at 200th iteration.

$$A_v = \int_{\Omega_{\mathbf{x}_{ls}}} B_{LS}(\mathbf{x}, \mathbf{x}_{ls}) \Big(1 - H\big(\phi(\mathbf{x}_{ls})\big) \Big) \, d\mathbf{x}_{ls} \tag{2.31}$$

$$B_{LS}(\mathbf{x}, \mathbf{x}_{ls}) = \begin{cases} 1, & |x^x - x_{ls}^x| < r_{ls}^x, |x^y - x_{ls}^y| < r_{ls}^y, |x^z - x_{ls}^z| < r_{ls}^z \\ 0, & \text{otherwise} \end{cases} \tag{2.32}$$

where, r_{ls}^x, r_{ls}^y, and r_{ls}^z are the length of x, y, and z axis of the prolate prolate spheroid mask. $(x_{ls}^x, x_{ls}^y, x_{ls}^z)$ and (x^x, x^y, x^z) are the (x, y, z) components of spatial variables $\mathbf{x}_{ls}$ and $\mathbf{x}$ respectively.

Stopping Boundary(2D algorithm) or Surface(3D algorithm) Based Energy (ξ_{SB}).

Cross sectional ultrasound images of the carotid artery often have shadowing and poor boundary contrast near lateral edges. There is a possibility of over segmentation and leaking through these regions if a proper stopping criterion is not used. We defined a stopping boundary (2D algorithm) or surface(3D algorithm) based energy ξ_{SB} that will

act as a stopping criterion. A stopping boundary is generated by doing 2D cubic spline interpolation from the initial points (red contour in figure 2.18a). A triangular stopping surface (figure 2.9c) was generated from interpolated initial points for 3D segmentation algorithm. Then, a binary mask $\phi_{sb}(\mathbf{x})$ having negative values inside the stopping boundary or surface and positive values outside the boundary or was generated. ξ_{SB} will stop the change of sign of the evolving LSF $\phi(\mathbf{x})$ at the stopping boundary or surface by replacing the values with high negative values. The evolving contour or mesh will never cross the stopping boundary (figure 2.18b) or surface (figure 2.9c). There will be no movement of the evolving contour or mesh when it touches the stopping boundary (region marked by white arrow in figure 2.18a) or surface but the contour or mesh can propagate in other direction. Figure 2.18b shows the final segmented boundary.

$$\xi_{SB} = \int_{\Omega} \delta(\phi(\mathbf{x})) B_{sb}(\mathbf{x}) \ d\mathbf{x} \tag{2.33}$$

where

$$B_{sb}(\mathbf{x}) = \begin{cases} 1, & \phi_{sb}(\mathbf{x}) > 0 \ (LIB) \ or \ \phi_{sb}(\mathbf{x}) < 0 \ (AWB) \\ 0, & \text{otherwise} \end{cases} \tag{2.34}$$

The level set evolution equation was found by taking first derivatives of R_p (equation 2.14), ξ_{ext}^{AWB} (equation 2.18), and ξ_{ext}^{LIB} (equation 2.16).

Level Set Evolution Equation for AWB Segmentation

$$\frac{\partial \phi_{AWB}(\mathbf{x})}{\partial t} = \mu_{AWB} div\left(\frac{p'(|\nabla\phi|)}{|\nabla\phi|}\right) + \delta\phi(\mathbf{x})\left\{\lambda_{AWB} div\left(g\frac{\nabla\phi}{|\nabla\phi|}\right) + \alpha_{LIB}g +\right.$$

$$\gamma_{AWB}\int_{\Omega_{\mathbf{x}_l}} B_{LR}(\mathbf{x},\mathbf{x}_l)\left(u_x - v_x\right)\left[\frac{I(\mathbf{x}_l) - u_x}{A_u} + \frac{I(\mathbf{x}_l) - v_x}{A_v}\right] d\mathbf{x}_l + \qquad (2.35)$$

$$\left.\sigma_{AWB}B_{ef}(\mathbf{x}) + \beta_{AWB}B_{sb}(\mathbf{x})\right\} \qquad\qquad \text{for 2D algorithm}$$

$$\frac{\partial \phi_{AWB}(\mathbf{x})}{\partial t} = \mu_{AWB} div\left(\frac{p'(|\nabla\phi|)}{|\nabla\phi|}\right) + \delta\phi(\mathbf{x})\left\{\lambda_{AWB} div\left(g\frac{\nabla\phi}{|\nabla\phi|}\right) + \alpha_{LIB}g +\right.$$

$$\gamma_{AWB}\int_{\Omega_{\mathbf{x}_l}} B_{LR}(\mathbf{x},\mathbf{x}_l)\left(u_x - v_x\right)\left[\frac{I(\mathbf{x}_l) - u_x}{A_u} + \frac{I(\mathbf{x}_l) - v_x}{A_v}\right] d\mathbf{x}_l + \qquad (2.36)$$

$$\left.\rho_{AWB}\left(A_v(\mathbf{x}) - A_u(\mathbf{x})\right) + \beta_{AWB}B_{sb}(\mathbf{x})\right\} \qquad\qquad \text{for 3D algorithm}$$

Level Set Evolution Equation for LIB Segmentation

$$\frac{\partial \phi_{LIB}(\mathbf{x})}{\partial t} = \mu_{LIB} div\left(\frac{p'(|\nabla\phi|)}{|\nabla\phi|}\right) + \delta\phi(\mathbf{x})\left\{\lambda_{LIB} div\left(g\frac{\nabla\phi}{|\nabla\phi|}\right) + \alpha_{LIB}g +\right.$$

$$\gamma_{LIB}\int_{\Omega_{\mathbf{x}_l}} B_{LR}(\mathbf{x},\mathbf{x}_l)\left(u_x - v_x\right)\left[\frac{I(\mathbf{x}_l) - u_x}{A_u} + \frac{I(\mathbf{x}_l) - v_x}{A_v}\right] d\mathbf{x}_l + \qquad (2.37)$$

$$\left.\nu_{LIB}\left(I(\mathbf{x}-u)^2 - I(\mathbf{x}-v)^2\right) + \beta_{LIB}B_{sb}(\mathbf{x})\right\}$$

where A_u and A_v are the local interior and exterior regions respectively for the calculation of local regional energy and are defined as [66]

$$A_u = \int_{\Omega_{\mathbf{x}_l}} B_{LR}(\mathbf{x},\mathbf{x}_l)H(\phi(\mathbf{x}_l))\ d\mathbf{x}_l \qquad (2.38)$$

$$A_v = \int_{\Omega_{\mathbf{x}_l}} B_{LR}(\mathbf{x}, \mathbf{x}_l)(1 - H(\phi(\mathbf{x}_l))) \ d\mathbf{x}_l \tag{2.39}$$

The level set evolution equation was implemented with a simple finite difference scheme having fixed space steps $\Delta x = \Delta y = 1$. The discretized form of time dependent LSF $\phi(x, y, t)$ is $\phi_{i,j}^k$ where (i, j) are the spatial indices and k is the time index. The temporal partial derivatives $\frac{\partial \phi_{LIB}(\mathbf{x})}{\partial t}$ or $\frac{\partial \phi_{AWB}(\mathbf{x})}{\partial t}$ were approximated by forward difference. The Eq. (2.36) or (2.37) can be expressed as

$$\phi_{i,j}^{k+1} = \phi_{i,j}^k + \Delta t \ L(\phi_{i,j}^k) \tag{2.40}$$

where $L(\phi_{i,j}^k)$ is the right hand side of evolution equation Eq. (2.36) or (2.37).

2.2.4 Stopping Criteria

If the stopping criteria fails to stop propagation of evolving contour, it may happen that the evolving contour for ECA and ICA will intersect instead of being separated because the contrast difference between ICA and ECA boundary is very poor due to its deep location. We define a new stopping criterion which is a combination of stopping boundary based energy function (equation. (2.33)) and changes in modified Haussdorf distance (MHD) between contours at successive iterations. The stopping boundary based energy function will stop the evolving contour at the boundary. It may happen that the evolving contour reaches the boundary long before maximum iteration number if we use only the stopping boundary based energy as a stopping criteria. We combined changes in MHD between successive iterations with stopping boundary based energy to save computational time by stopping the contour evolution when it reaches the boundary. We also implemented following stopping criteria to compare the performance of our novel stopping criterion.

1. Percentage change in area inside the contours at successive iterations. [33]
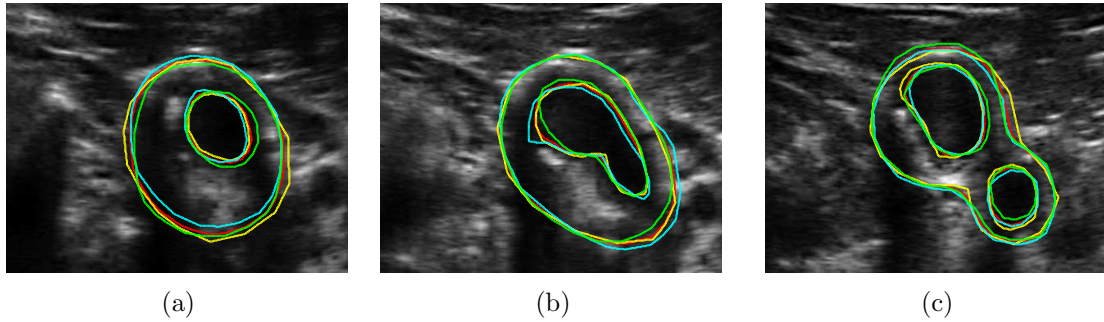
Figure 2.19: . Ground truth boundary was generated by computing average curve from manual segmentation. Ground truth boundary for sample images at (a) Common carotid artery (b) Carotid bulb (c) Internal and external carotid artery region. Green, yellow, and blue color represent manual segmentation and red color represents ground truth boundaries.

2. Change in MHD between contours at successive iterations (LIB) or every fourth iterations (AWB).

Changes in MHD between contours never has been used as a stopping criterion. However, Cohen *et al.* [47] used the norm distance between two curves at successive iterations for snake models as a stopping criterion. The computational burden is very high for finding the corresponding points to calculate norm distance for the level set method which will eventually slow down the curve evolution.

2.3   Ground Truth Boundary Computation

In absence of histology images or CT angiography images, an average curve was generated from manually segmented boundaries by three observers and it was used as a ground truth boundary (figure 2.19). The accuracy of the segmentation algorithm was calculated by comparing against this ground truth boundary and precision was computed by evaluating the reproducibility of the algorithm generated boundaries. A manual image segmentation protocol was developed based on consensus among multiple observers using a set of training volumes. Three observers segmented LIB and AWB on the selected slices for each subject. Total 210 2D cross-sectional slices were extracted from 10 3D US images. The Stradwin [1] was used for manually outlining the ultrasound volumes. The expert also chose seven initial
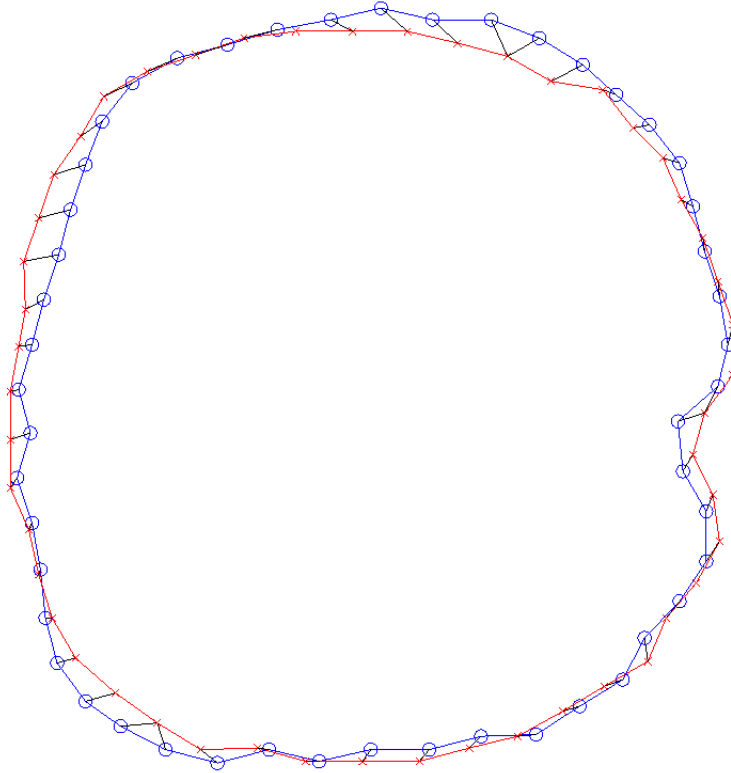
Figure 2.20: Connecting Black line shows the correspondence between points.

points on each boundary three times on each cross sectional images with a week between repetitions on the same data set.

Given a set of N curves $X_1, X_2, \cdots, X_N$, each with n equidistance points, we found the average curve Y by first finding contour correspondence using the ant colony optimization method [69]. The advantages of using this method for finding contour correspondence is that the contour correspondence is formulated as quadratic assignment problem (QAP) incorporating proximity information and better matching result was found due to the neighborhood relation between points. Figure 2.20 shows the correspondence between points on two boundaries. We randomly chose one curve X_1 and found the correspondence with all other curves. A point x_{11} on curve X_1 corresponds to points $x_{21}, x_{31}, \cdots, x_{N1}$ on each curve $X_2, X_3, \cdots, X_N$ and similar notation is used for remaining n-1 points i.e., the point x_{21} corresponds to points $x_{22}, x_{32}, \cdots, x_{N2}$.

A point on the average curve is the centroid of the N corresponding points

$$y_i = \frac{1}{N} \sum_{j=1}^{N} x_j i \tag{2.41}$$

Fig. 2.19 shows ground truth boundaries for LIB and AWB for three representative sample images at CCA, bulb, and ICA regions of the carotid artery.

Chapter 3: Evaluation Criteria

We used volume based, region based, and boundary distance based metrics to evaluate our proposed algorithm. Volume based metrics have clinical interest whereas region based and boundary distance based metrics capture finer details about computer segmentation with respect to manual segmentation. We used percentage VWV difference (ΔVWV) and absolute VWV difference ($| \Delta VWV |$) as volume based metrics. VWV difference (ΔVWV) for ith subject is defined as

$$\Delta VWV^i = \frac{\overline{VWV^i_{computer}} - \overline{VWV^i_{hand}}}{\overline{VWV^i_{hand}}} \times 100\%$$
(3.1)

where, $\overline{VWV^i_{hand}}$ and $\overline{VWV^i_{hand}}$ are the mean VWV measurement from repeated measurements of VWVs from computer-generated and hand-outlined boundaries. The mean ΔVWV gives the overall disagreement in 3D US data set

$$\overline{VWV} = \frac{\sum_{i=1}^{N} \Delta VWV^i}{N}$$
(3.2)

where, N=10 is the total 3D US images.

Minimal Detectable Change (MDC) [70] was computed to find the smallest amount of change of VWV that can be detected by algorithm. The equation for calculating MDC [70] at 96% confidence interval is

$$MDC_{96} = 1.96 \times \sqrt{2} \times SEM$$
(3.3)

45

where, SEM [71] is standard error of measurements which is calculated as follows

$$SEM = sd \times \sqrt{1 - r} \qquad (3.4)$$

where sd is the standard deviation of the measurement, and r is the reliability coefficient(test-retest reliability in the form of intra-class correlation coefficient).

Coefficient of variation(COV) was used to compare the reproducibility of the algorithm and manual computed VWV and it is defined as

$$COV = \frac{\overline{SD}}{\overline{VWV}} \times 100\% \qquad (3.5)$$

where $\overline{VWV} = \frac{\sum_{i=1}^{N} \overline{VWV^i}}{N}$ and $\overline{SD} = \sqrt{\frac{\sum_{i=1}^{N} (\overline{SD^i})^2}{N}}$. standard deviation SD^i was computed from the repeated measurements of VWV for each 3D US image.

Dice similarity coefficient (DSC), a region based measure, is the area overlap of two boundaries and is defined as follows

$$DSC = 2 \frac{\mid R_{hand} \bigcap R_{computer} \mid}{\mid R_{hand} \mid + \mid R_{computer} \mid} \qquad (3.6)$$

where R_{hand} and $R_{computer}$ are the region enclosed by hand-outlined and computer-generated boundaries.

We used Hausdorff distance (HD)[72] and modified HD (MHD)[57] as boundary distance based measurements to compare algorithm and hand-outlined boundaries. HD finds the most mismatched points between two contours, which is defined as follows for two finite point sets A and B

$$H(A, B) = max\,(h(A, B), h(B, A)) \qquad (3.7)$$

where

$$h(A, B) = \max_{a \epsilon A} \min_{b \epsilon B} \|a - b\| \qquad (3.8)$$

and $\|a - b\|$ denotes Euclidean norm on points of A and B. One single mismatched point is enough to make HD very high between two curves. MHD considers the contribution of all points in curve mismatching and Eq. (3.8) is defined as follows for MHD:

$$h(A, B) = \frac{1}{N_a} \sum_{a \epsilon A} \min_{b \epsilon B} \|a - b\| \tag{3.9}$$

We also computed william index (WI)[73] which is the ratio between average computer to observer agreement and the average interobserver agreement. Given (n+1) observers numbered from 0 to n do segmentation on N images, WI compares observer 0 (computer generated segmentation) with the reference group of n observers (manual segmentation). WI is defined as [73]

$$I = \frac{\frac{1}{n} \sum_{j=1}^{n} \frac{1}{D_{0,j}}}{\frac{1}{n(n-1)} \sum_j \sum_{j':j' \neq j} \frac{1}{D_{j,j'}}} \tag{3.10}$$

where $D_{j,j'}$ is the average disagreement between two observers j and j' computed on N images.

The jacknife estimate of standard error in the computation of the WI is given by [73]

$$se = \left\{ \frac{1}{N-1} \sum_{i=1}^{N} [I_i - \bar{I}]^2 \right\}^{1/2} \tag{3.11}$$

where $\bar{I} = \frac{1}{N} \sum_{i=1}^{N} I_i$ and I_i is WI computed by removing ith image from total N images. Thus the 95% CI for the estimate of the WI is

$$\bar{I} \pm Z_{0.95} se \tag{3.12}$$

where $Z_{0.95} = 1.96$ is the 95th percentile of the standard normal distribution.

Friedman's two-way analysis of variance by ranks [74] is computed to find the statistical

difference between three different stopping criteria. It is a nonparametric procedure where errors due to different stopping criteria are ranked for each data set. The test statistic is defined as

$$\chi^2_{m-1} = \frac{12}{Nm(m+1)} \sum_{j=1}^{m} R_j^2 - 3N(m+1) \tag{3.13}$$

where, N, m, and R_j represent number of data sets (N=210 cross sectional images), number of stopping criteria (m=3) and sum of ranks for jth stopping criterion respectively. The statistic is compared against χ^2 distribution of m-1 degrees of freedom to determine rejection or acceptance of null hypothesis. The rejection of null hypothesis represents a significant difference in the rank i.e. the stopping criteria performs differently.

Chapter 4: Results and Discussion

We evaluated algorithm accuracy and reproducibility using 210 cross sectional images from 10 3D US images. 3D segmentation algorithm was validated by slicing the algorithm-segmented surface on the same planes as the manual segmentation and comparing the resulting boundaries with the ground truth boundaries in 2D. The whole volume was divided into two regions: from bifurcation to proximal CCA (`BF_ 2 _CCA`) and from bifurcation to distal ICA (`BF_ 2 _ICA`) to find the performance at these regions separately. The image contrast is completely different in these two regions. There is a possibility of compensating low performance at ICA by high performance of algorithm at CCA if whole volume is used for comparison. This chapter is divided into four section: thresholds of stopping criteria (section 4.1) , weights parameters of DRLSE (section 4.2) , comparison of different stopping criteria (section 4.3) , and evaluation of our proposed 2D and 3D algorithm (section 4.4) .

4.1   Thresholds of Stopping Criteria

In our level set evolution method, we segmented LIB and AWB simultaneously. Level set evolution will be unstable if LIB and AWB evolving contour touches each other. We put a constraint for level set evolution when we used other two conventional stopping criteria. The constraint is that LIB and AWB will always maintain 0.8 mm distance from each other because LIB and AWB are separated by carotid intima, media, and adventitia layer [75]. Following steps were used to find stopping metric value for each stopping criteria.

1. Performed the level set evolution without any stopping criteria and found the iteration number when evolving contour reaches the boundary (green contour in figure 4.1a).

2. Plotted the stopping metric with respect to iteration number and found the iteration number when the rate of change in metric slows down (175th iteration in figure 4.1b).
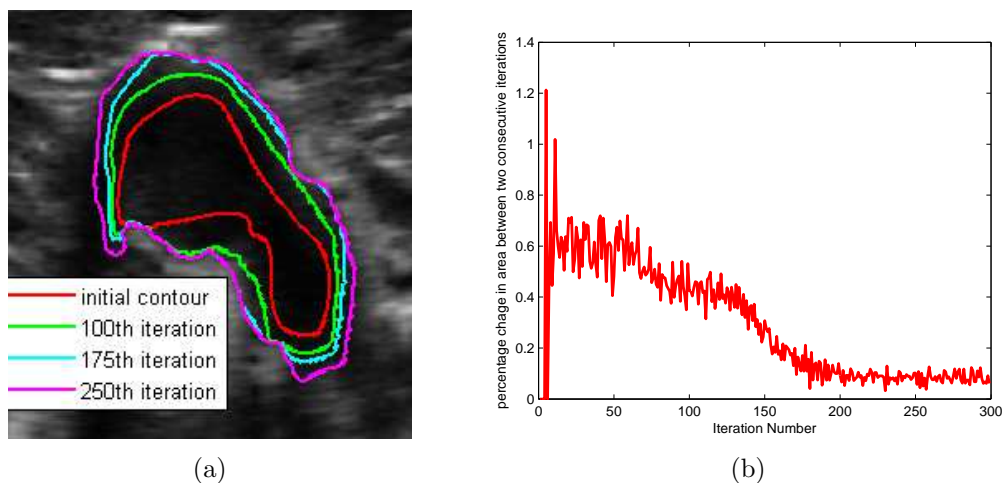
Figure 4.1: (a)Evolving contour at 0th, 100th, 175th and 250th iteration without any stopping criteria. Evolving contour reaches LIB boundary at 100th iteration (green contour). After 100th iteration, contour propagate only through poor boundary contrast and shadowing. (b) Percentage change of area between two consecutive iteration vs iteration numbers.

3. Stopping threshold value will be average of the metric value at iteration number found on step (2) and (1). According to figure 4.1, the stopping metric will be 0.3.

We selected 30 representative cross sectional slices from 10 subjects at BF₋ 2 ₋CCA and BF₋ 2 ₋ICA regions because the size of artery is very different at those regions. We applied above procedure on all selected images to find stopping threshold for all stopping criteria. The final threshold will be the mean of stopping metric value found for 15 cross sectional slices at each region. Table. 4.1 shows the threshold value at BF₋ 2 ₋CCA and BF₋ 2 ₋ICA

Table 4.1: Threshold value for different stopping criteria at bifurcation to proximal CCA (BF₋ 2 ₋CCA) and bifurcation to distal ICA (BF₋ 2 ₋ICA) regions for LIB and AWB segmentation.

Stopping Criteria (SC)	Boundary Name	BF₋ 2 ₋CCA	BF₋ 2 ₋ICA
Change in MHD for Proposed SC (mm)	LIB	0.06	0.07
	AWB	0.8	0.9
% Change in Area	LIB	0.2	0.3
	AWB	0.1	0.2
Change in MHD (mm)	LIB	0.07	0.09
	AWB	.15	.24

50

for LIB and AWB for all stopping criteria.

For 3D segmentation algorithm, We used percentage change of pixels that alter their locations relative to evolving surface. As the evolution of the surface is progressing, pixels will change their location from interior to exterior of the evolving surface (AWB) or from exterior to interior of the evolving surface (LIB). We calculated percentage change of pixel locations at each iteration. If the percentage change of pixel locations is less than 10% (LIB) or 8% (AWB) for consecutive 5 iterations, then the evolution will be terminated.

4.2 Weight Parameters of DRLSE

The weight parameters in eqution (2.36) or (2.37) has significant role in the contour evolution. Since the length parameters $\lambda_{LIB/AWB}$ is not very sensitive, it was fixed to 1 (LIB) and 5 (AWB) to make contours smooth. The time step Δt must satisfy the courant-Friedreich-Lewy (CFL) condition $\mu \Delta t < (1/4)$ for numerical stability and $\mu = 0.1$ and $\Delta t = 4.0$ was used in this paper. The non zero value of $\alpha_{AWB/LIB}$ gives additional external force to drive the motion of contour. A large value of $\alpha_{AWB/LIB}$ will cause leakage through the weak boundaries. As our novel stopping criterion stops the leakage of evolving contour, we can set the $\alpha_{AWB/LIB}$ to a high value. But we set to $\alpha_{AWB/LIB} = 5.0$ to compare the performance of other stopping criteria. The ellipse fitting energy or stopping boundary based energy is a kind of step function. It only looks for spatial variables which are close to these boundary and change the sign of evolving LSF $\phi \mathbf{x}$ for the pixel which are outside the boundary. So parameters σ_{AWB} and $\beta_{AWB/LIB}$ are not very sensitive and they were fixed to 2. We found the parameters for region based energy (ξ_{LR} or ξ_{GR}) by holding other parameters to their fixed value and changing $\Gamma_{LIB/AWB}$ and ν_{LIB} to a range of values at a time for 50 images. The parameters value which gives the highest dice similarity coefficient (DSC) are selected as final value. Table 4.2 summarizes the optimized value of all parameters. Same values were used for 2D and 3D segmentation.

Table 4.2: Optimized parameters value for LIB and AWB segmentation

Parameter's Name	LIB			AWB		
	Symbol	Value		Symbol	Value	
		2D	3D		2D	3D
Time step	Δt	4	10	Δt	4	10
Regularized Constant	μ_{LIB}	0.025	0.005	μ_{AWB}	0.025	0.005
Length Weight	λ_{LIB}	1	1	λ_{AWB}	5	0.5
Area Weight	α_{LIB}	5	15	α_{AWB}	5	20
Local Region Radius	r	1.5 mm	1.5 mm	r	1.7 mm	1.7 mm
Local Region Weight	γ_{LIB}	0.5	2	γ_{AWB}	0.5	-5
Global Region Weight	ν_{LIB}	0.5	0.5	NA	-	-
Ellipse Fitting Weight	NA	-	-	σ_{AWB}	2	2
Local Smoothness Radius	NA	-	-	r_{ls} $(r_{ls}^x, r_{ls}^y, r_{ls}^z)$	-	(1.7,1.7,2)mm
Local Smoothness Weight	NA	-	-	ρ_{AWB}	-	5
Stopping Boundary or Surface Weight	β_{LIB}	2	2	β_{AWB}	2	2

4.3 Comparison Between Proposed and Conventional Stopping Criteria

To compare the performance of three different stopping criteria, all weight parameters (Table 4.2) of level set evolution algorithm were kept constant. The same initial contour was used for all three stopping criteria and level set evolution was carried out separately for these three stopping criteria. Algorithm-generated boundaries using these three stopping criteria were compared against ground truth boundaries.

(a)

(b)

53

(c)
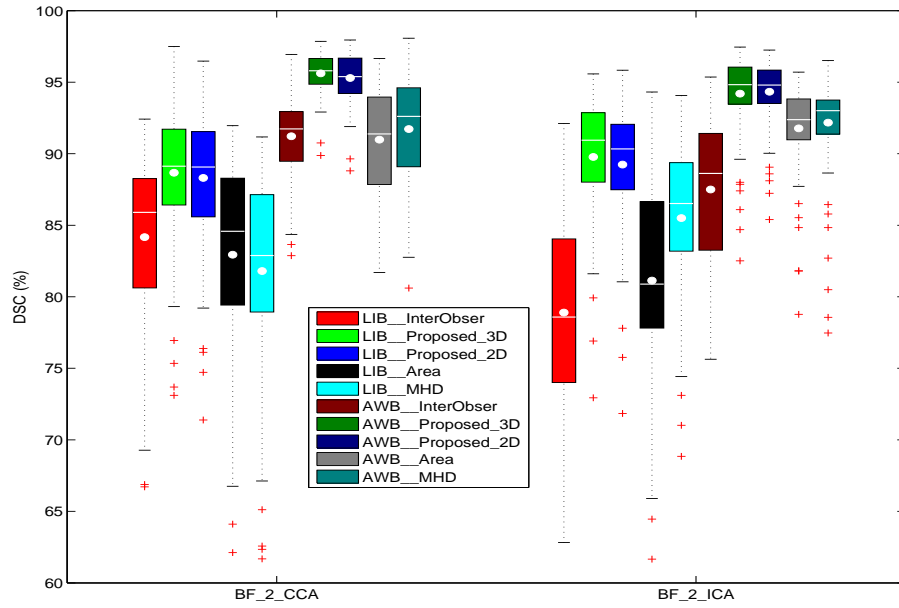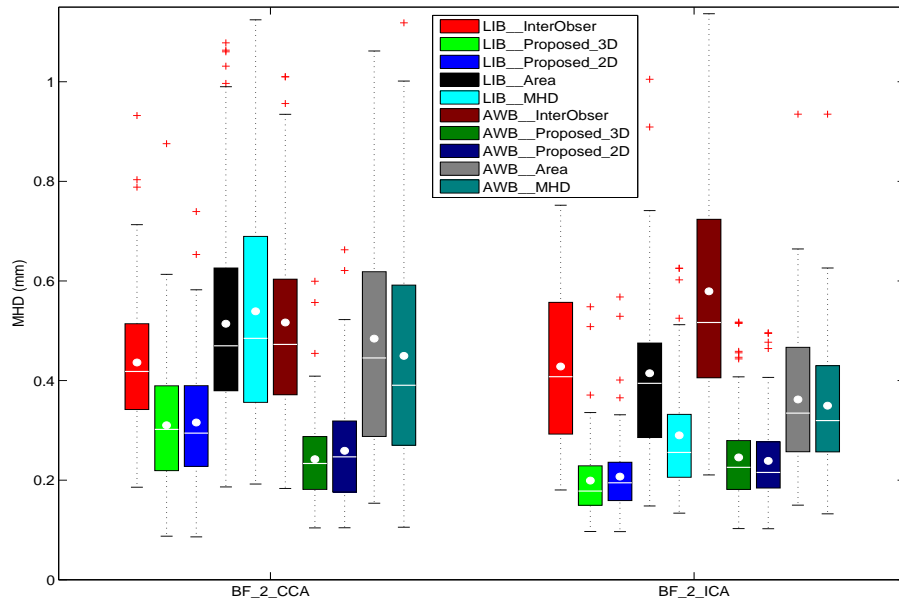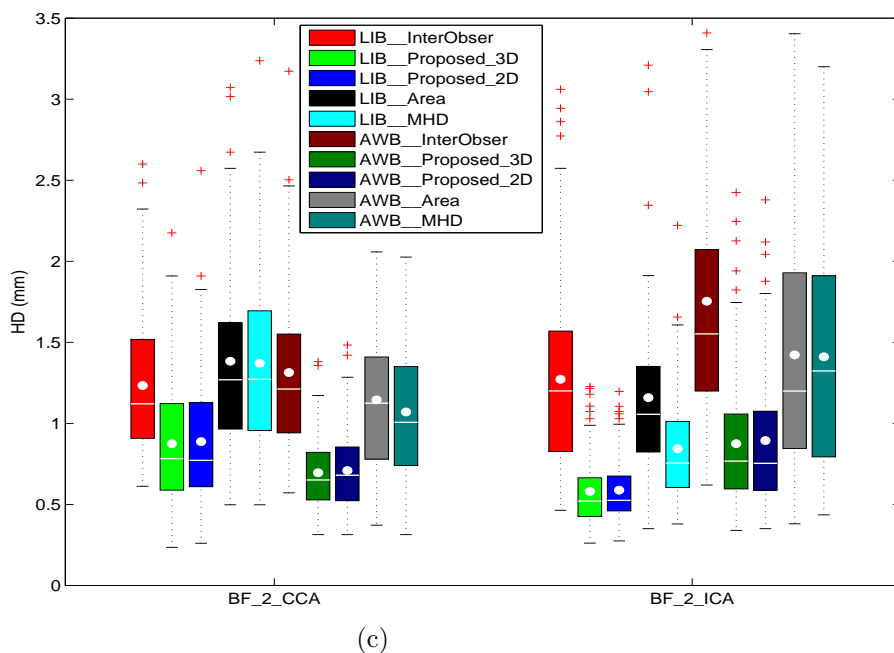
Figure 4.2: Boxplots of the (a) DSC , (b) HD , (c) MHD between algorithm-generated boundaries and ground truth boundaries for three different stopping criteria for segmenting LIB and AWB. It also shows the performance of manual segmentation of three observers in terms of inter-observers variability. The white line inside box represents median, the white circle represents mean, the edge of box represents 25th and 75th percentiles, the whiskers extend to the most extreme data points not considering outliers, and red (+) represents outliers.

Figure 4.2 shows the performance of three different stopping criteria for the segmentation of LIB and AWB in terms of DSC, HD and MHD. It also shows inter-observer performance of manual segmentation with the performance of proposed 3D segmentation. The performance was compared in the bifurcation to proximal CCA(`BF_ 2 _CCA`) and bifurcation to distal ICA(`BF_ 2 _ICA`) regions separately. The performance of proposed stopping criterion is better than other two stopping criteria. Other two stopping criteria failed to stop leaking through poor boundary contrast region. As LIB and AWB was segmented simultaneously, wrong segmentation of LIB affected segmentation of AWB. But our proposed stopping boundary based energy function was able to stop leaking through the poor boundary contrast regions.

DSC value (figure 4.2a) shows that the difference between 75th and 25th percentiles is higher for LIB than AWB segmentation by the proposed algorithm. But, MHD value

Table 4.3: Comparison of three different stopping criteria for the segmentation of LIB and AWB in terms of William Index (WI). The expected value of WI is 1.0.

Stopping Criteria	Boundary Name			
	LIB		AWB	
	WI	95% CI Low, High	WI	95% CI Low, High
Proposed	0.874	0.870, 0.878	1.035	1.03, 1.039
Change of Area	0.564	0.562, 0.567	0.686	0.682, 0.689
Change of MHD	0.619	0.615, 0.662	0.723	0.719, 0.727

(figure 4.2b) shows that the difference between 75th and 25th percentiles are similar for LIB and AWB segmentation. The reason for this discrepancy is that DSC is very sensitive to size and smaller objects are penalized more and get a much lower score than larger objects. The proposed algorithm performed better in segmenting LIB at `BF_ 2 _ICA` region and AWB at `BF_ 2 _ CCA` region.

Most of the complex plaques are situated in the `BF_ 2 _ CCA` regions. It may happen that wrong stopping boundary was generated for LIB due to interpolation at initialization step. AWB becomes very difficult to identify at `BF_ 2 _ CCA` region and algorithm performance depends on user initialization. HD value (figure 4.2c) also shows that one pixel in algorithm generated boundary is always far away from ground truth boundary at `BF_ 2 _ICA` region.

The Friedman's rank sum test indicated a significant difference between the performance of the three stopping criteria ($p < 0.001$) for segmenting LIB and AWB of carotid artery for both regions using these three error metrics. Multiple comparison showed that the proposed stopping criterion consistently outperformed the other two stopping criteria.

Table 4.3 shows the comparison between stopping criteria in terms William index (WI). We used only MHD as error metric to calculate WI for 2D segmentation algorithm because MHD does not depend on size of arteries. WI of the proposed 2D algorithm is close to 1 for both LIB and AWB segmentation. It means that the proposed algorithm agreed with the 3 manual observers as well as 3 manual observers agreed with each other. From figure 4.2, Friedman's rank sum test, and WI value, we can conclude that our proposed stopping

criterion is better than other two stopping criteria. Single threshold based stopping criteria will not able to stop over-segmentation and under-segmentation.

(a) -10 mm   (b) -8 mm   (c) -6 mm

(d) -4 mm   (e) -2 mm   (f) 0 mm

(g) 2 mm   (h) 4 mm   (i) 6 mm

(j) 8 mm   (k) 10 mm
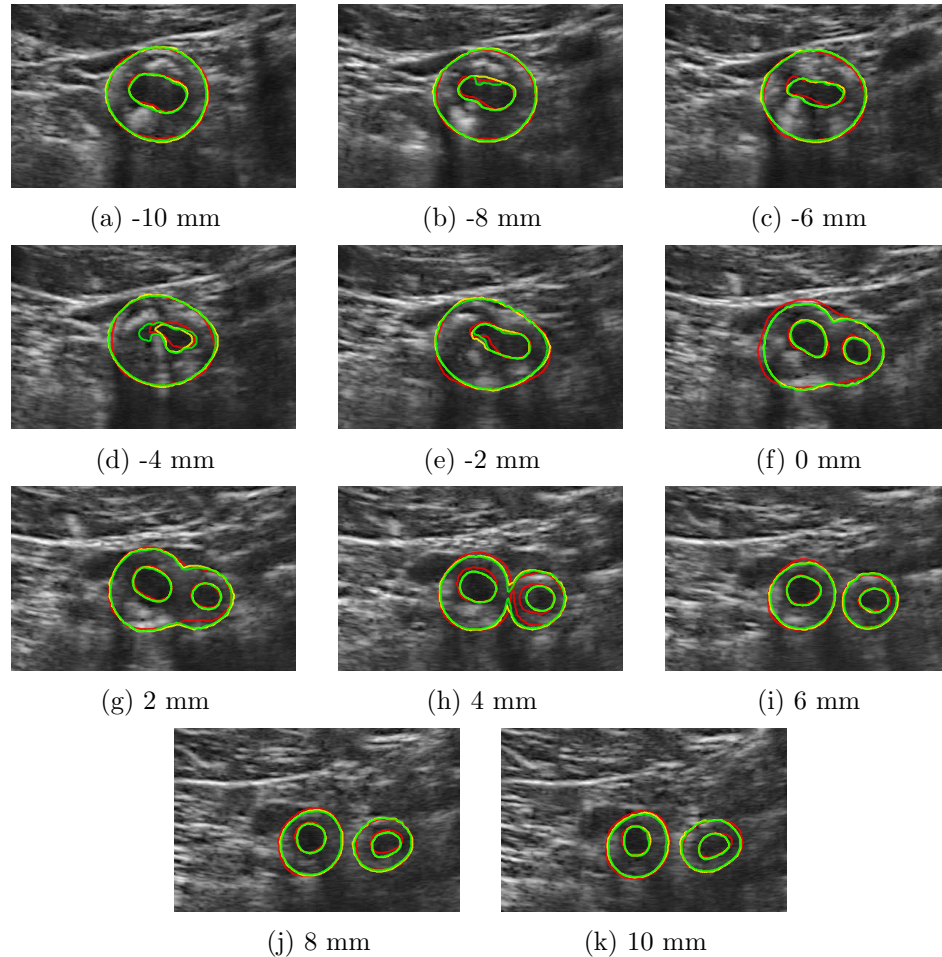
Figure 4.3: sample LIB and AWB segmentations in a single 3D US images by the proposed 2D segmentation (green contour) and 3D segmentation (yellow contour) algorithm . Red contour represents ground truth boundaries. Negative and positive distance represents towards CCA and ICA direction respectively with respect to bifurcation slice. Distance 0 represents 1st slice where CCC is bifurcated to ICA and ECA.

4.4 Performance of the Proposed Algorithm

This section discusses the performance of our proposed 2D and 3D algorithm in terms of clinical, boundary-based, and distance-based metrics in a greater detail. VWV is the difference between arterial volume (volume enclosed by AWB boundary) and luminal volume

(volume enclosed by LIB boundary). The volumes from 2D algorithm generated boundaries and ground truth boundaries were computed by first finding average area enclosed by the boundary of two consecutive cross-sectional slices, then multiplying this average area with the interslice distance of 1mm and adding this product for all slices. The final result of 3D segmentation algorithm is a surface. Volume was calculated directly from the surface. Figure 4.3 shows qualitative performance of proposed 2D and 3D segmentation algorithm.

4.4.1 Accuracy

We used Bland-Altman plots [76] to find the agreement between VWV generated ground truth and algorithm generated boundaries. Bland-Altman plots the differences between VWVs computed from ground truth boundaries (VWV_G) and algorithm-generated boundaries (VWV_A) versus their averages for each 10 3D US volumes. Figure 4.4a shows Bland-Altman plots for VWV generated from ground truth and algorithm generated boundaries with mean bias and 95% confidence interval of mean bias (mean bias $\pm$ 1.96 $\times$ standard deviation (SD) of the difference between VWVs from ground truth and algorithm generated boundaries). The mean bias for the 2D and 3D algorithm is -2.94 mm^3 and 49.3 mm^3. We can conclude that algorithm generated boundaries agree with hand-outlined boundaries as all data points are within 1.96 SD line.

We also used Pearson product-moment correlation analysis to find agreement between VWV from ground truth and algorithm-generated boundaries. [Fig. 4.4b] plots the VWV generated using the algorithm against the VWVs generated from ground truth segmentation. The Pearson correlation coefficient is $r = 0.99$ (2D segmentation algorithm) and $r = 0.97$ (3D segmentation algorithm) for $p < 0.001$ which shows two methods are highly significant for generating VWV. We also used Friedman's rank sum test on VWV generated from these two methods to find the statistical difference between them and p=0.53 from the test indicates that two methods are not statistically different.

The 95 % confidence interval (CI) of the mean difference between VWV generated from algorithm and ground truth segmentation was computed. The mean VWV difference
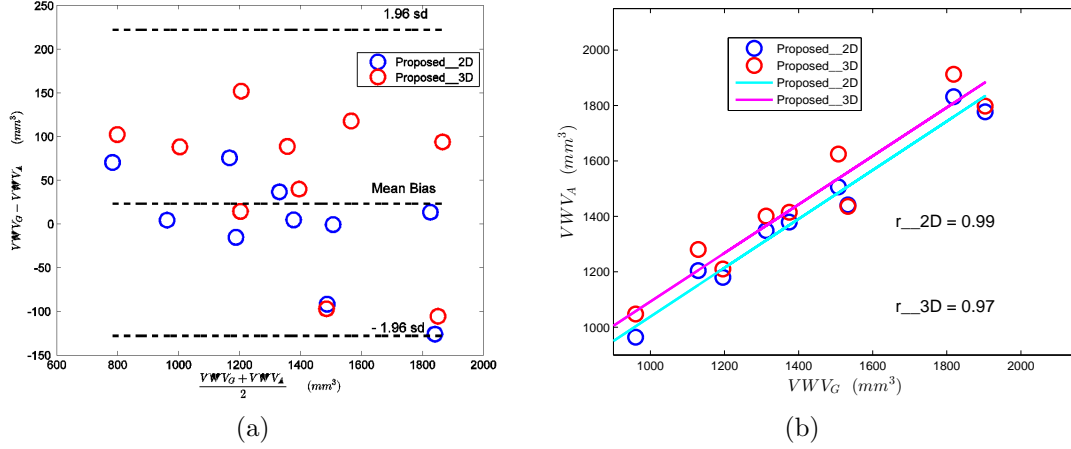
Figure 4.4: (a) Bland-Altman plots the difference between VWV computed from ground truth boundaries (VWV_G) and algorithm(2D and 3D)-generated boundaries (VWV_A) versus their averages for each patients. (b) Correlation plot of VWV computed from hand-outlined boundaries and algorithm(2D and 3D)-generated boundaries.

between these two methods was -2.94 mm^3 with a 95% CI of -107.9 mm^3 to 102.1 mm^3 for 2D segmentation algorithm and 4.93 mm^3 with a 95% CI of -95 mm^3 to 194.3 mm^3 for 3D segmentation algorithm. The 2D segmentation algorithm yielded a percentage volume difference (Equation 3.1) of 6.45 ± 4.93 and absolute volume difference ($\mid \Delta VWV \mid$) of 3.43 ± 3.42 whereas percentage volume difference and absolute volume difference for 3D segmentation algorithm are 4.82 ± 6.93 and 7.2 ± 4.04 . The MDC of VWV was 161 mm^3 (10.89% of mean VWV), 171.5 mm^3 (11.22% of mean VWV) and 222.16 mm^3 (21.2% of mean VWV) from repeated measurements of VWV by 2D segmentation algorithm, 3D segmentation algorithm and manual observers respectively.

4.4.2   Performance as a Function of Distance from Bifurcation

Figure 4.5 shows the performance of algorithm in terms of DSC, MAD and HD as a function of distance from BF for AWB and LIB segmentation. The circle represents mean value and the error bar represents one standard deviation above and below the mean. Negative and positive distance represents bifurcation to proximal CCA (`BF_ 2 _CCA`) and bifurcation to distal ICA (`BF_ 2 _ICA`) regions respectively. The performance of algorithm is better for

the segmentation of AWB than LIB at `BF_ 2 _CCA` region (figure 4.5). The segmentation accuracy is better for AWB than LIB at `BF_ 2 _ICA` region in terms of DSC (figure 4.5a, figure 4.5b) but LIB segmentation is better in terms of MHD (figure 4.5c, figure 4.5d). The reason for this discrepancy is that DSC is very sensitive to size of contour and at `BF_ 2 _ICA` region, artery consists of ECA and ICA. HD value (figure 4.5e, figure 4.5f) is higher of AWB than LIB segmentation at `BF_ 2 _ICA` region and opposite is true at `BF_ 2 _CCA`.

The algorithm performed better in segmenting AWB than LIB of CCA where as the performance was better in the LIB than AWB segmentation at `BF_ 2 _ICA` region (figure 4.5) Most of the plaques situated at distal CCA and the shape of LIB sometimes are very complex at the presence of plaque. The performance of proposed stopping criteria depends on stopping boundary which was generated from boundary points initialized by users. Sometimes six points are not enough to capture complex LIB shape. Algorithm-generated boundary was compared against manually boundary. Manually segmented boundary can easily become more complex than algorithm-generated boundary. We used inter-slice distance (ISD) of 4mm for initialization of points. A spline interpolation was used to find the initialization on other slices because we assume that there will no abrupt change in plaque boundary within 4mm. But, sometimes manual observers were confused by artifacts and found abrupt change in plaque shape within ISD of 3mm. Due to deep location of ICA and ECA, it is difficult to identify AWB than LIB of ICA and ECA. Edge strength is not too high for AWB in this region. The final boundary largely depends on region based energy and stopping boundary. Most of the variability in segmenting AWB at `BF_ 2 _ICA` region comes from user initialization.

Two ellipses are fitted through ICA and ECA. If there is a intersection between ellipses fitted through ICA and ECA, there will be single AWB boundary where as manual observers can easily separate ICA and ECA [Fig. 4.3].
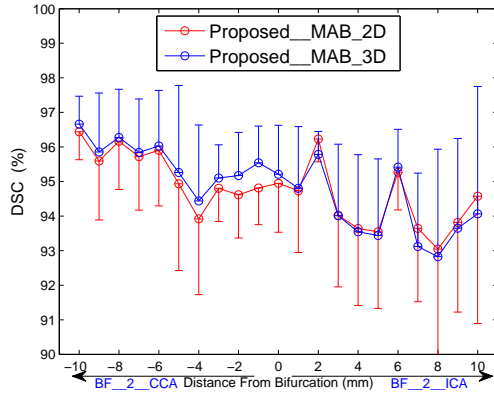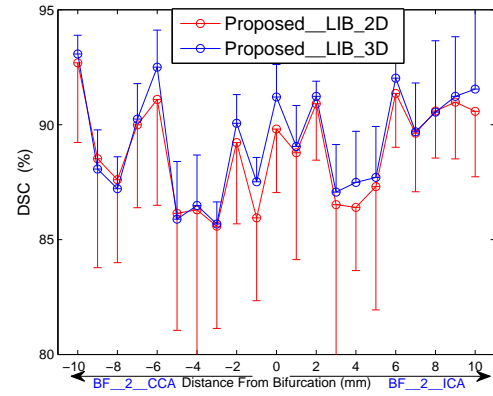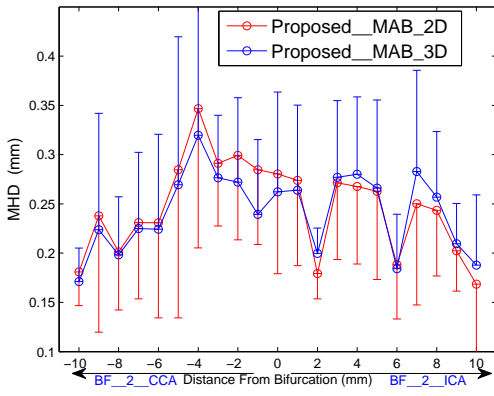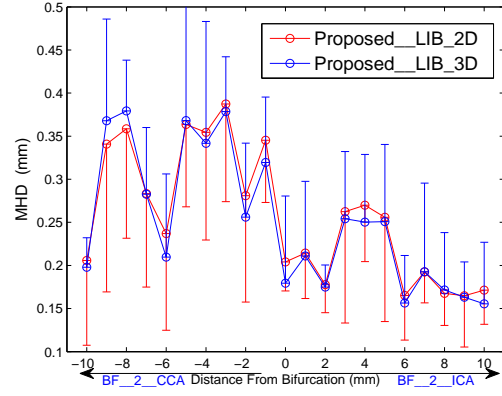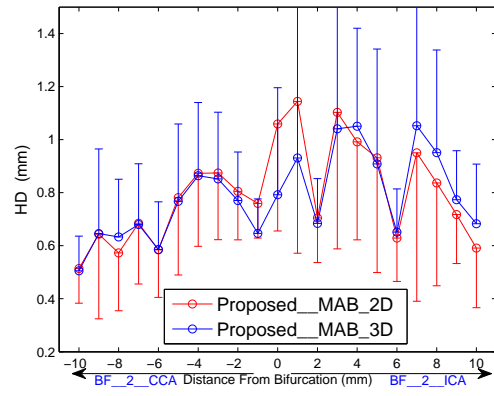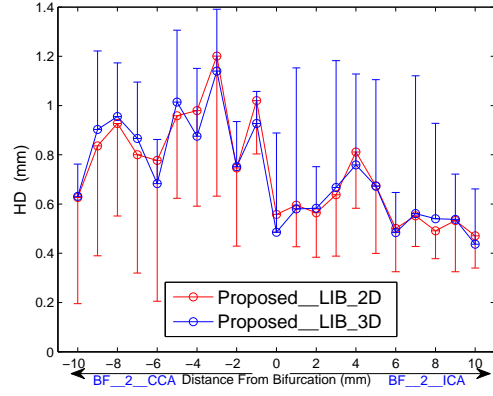
Figure 4.5: Performance of algorithm as function of distance to the BF for the AWB and LIB. The error bar and circle is mean and standard deviation respectively. Negative and positive distance represents bifurcation to proximal CCA (`BF_ 2 _CCA`) and bifurcation to distal ICA (`BF_ 2 _ICA`) regions respectively.

These are the reasons for performance difference of proposed algorithm for the segmentation of LIB and AWB in `BF_ 2 _CCA` and `BF_ 2 _ICA` regions. Our hypothesize is that more points for initialization and reduced ISD will increase the performance of the algorithm and radiologist are opted to any number of points and any ISD depending on plaque shape in clinical settings.

4.4.3   Performance of Each Point on the Boundary

Though MHD gives average distance between corresponding points of two curves, it does not provide distance between each corresponding points. Figure 4.6a,4.6a show a graphical way of showing distance between corresponding points of algorithm generated and ground truth boundaries for a single 3D volume. Positive and negative distance for a point represent over-segmentation and under-segmentation respectively. Over- and under- segmentation mean point in algorithm-generated boundary is outside and inside of ground truth boundary respectively. The closest points were considered corresponding points. 3D volumes were generated by stacking all 21 slices for each 3D US images. Figure 4.6d shows distribution of distance between corresponding points of algorithm generated and ground truth boundaries for all 10 volumes (210 cross-sectional slices). The 95% confidence interval of mean is (-0.2466, 0.2305) for LIB and (-0.2464,0.2550) for AWB by the 2D segmentation algorithm and the 3D segmentation algorithm yielded 95% confidence interval of mean (-0.2422, 0.2460) for LIB and (-0.2020,0.2869) for AWB. Our algorithm can detect plaque thickness change if change is more than -.48 mm to 0.48 mm.

4.4.4   Intra- and Inter-observer Variability

We used COV to find the intra- and inter-observer variability of algorithm and manual observers in calculating VWV. We calculated VWV three times using our algorithm on 10 subjects (N=10). The algorithm gave a COV of 5.2%. Two observers initialized the points for algorithm twice and we calculated inter-observer variability from these measurements. Three manual observers segmented the boundaries. The COV for inter-observer segmentation
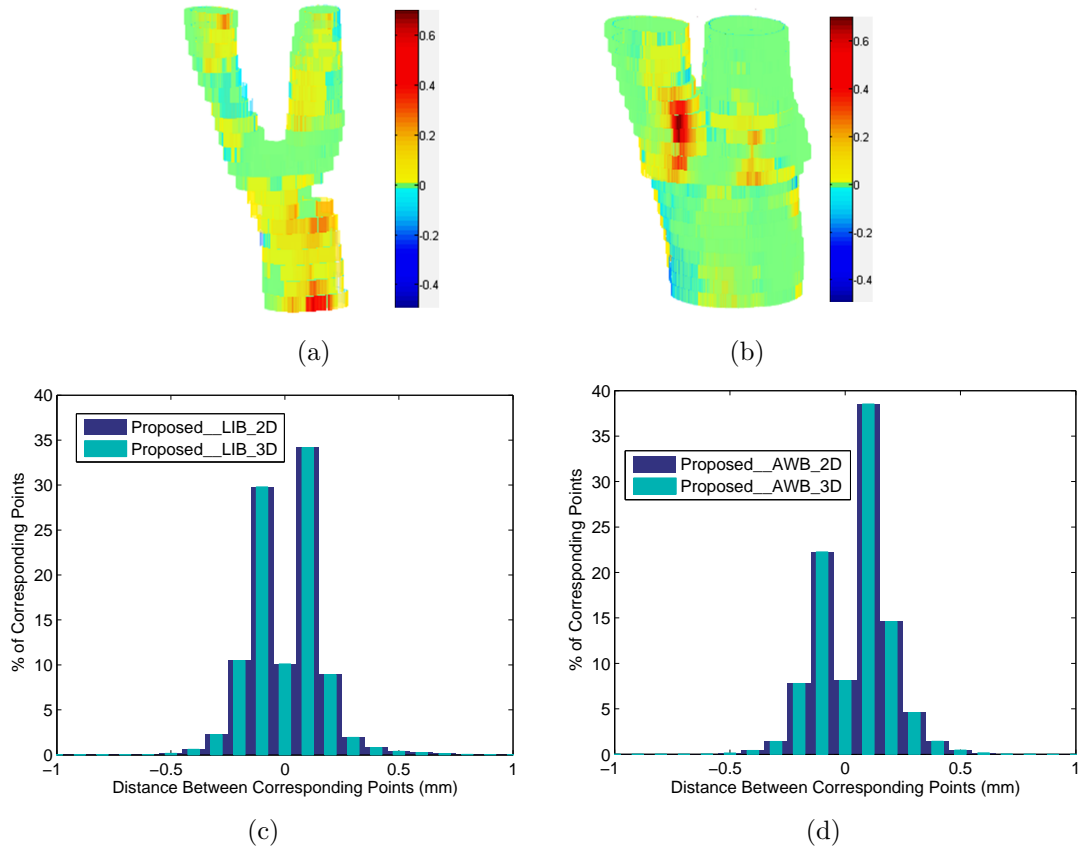
Figure 4.6: Distance between corresponding points of algorithm-generated and ground truth boundaries for (a) LIB and (b) AWB where positive and negative distance represents over- and under-segmentation respectively. The frequency distribution of distance between corresponding points of c) LIB and d) AWB.

is 11.28% and 16.52% by algorithm and manual observers respectively. We also used Friedman's rank sum test on VWVs generated from these repeated measurements to find the statistical significance difference between them. p-value from the Friedman's rank sum test indicated that there was no significant difference between inter- and intra- observers measurements by algorithm and manual observers.

4.4.5 Execution Time

The time for segmenting LIB and AWB was calculated using 210 cross-sectional images for 10 subjects. Three observers segmented LIB and AWB manually. 5 ± 1 min was required to segment the LIB and AWB for a single 2D cross-sectional slices. Due to

poor boundary contrast, more time is required to segment LIB and AWB at ICA than at CCA. The algorithm takes 9 ± 1.2 min of computational time to initialize seven points for seven cross-sectional 2D slices of a single 3D US images. The algorithm, implemented in MATLAB(Natick,MA) without any optimization, took 1 ± 0.2 min to segment LIB and AWB of a single 2D cross-sectional slice on a desktop with an Intel core 2 duo processor and 4 GB of RAM. The overall execution time to segment whole volume is 40 ± 5 min, 45 ± 5 min and 100 ± 5 min for 2D segmentation algorithm, 3D segmentation algorithm, and manual observers respectively. Further optimization and implementation in C can significantly speed up the computation time.

Chapter 5: Conclusion and Future Works

There are several challenges to develop a robust semiautomatic segmentation algorithm for segmenting wall of atherosclerotic carotid arteries using *in vivo* 3D ultrasound images . The contrast is poor at boundaries parallel to ultrasound beams in carotid images. Due to presence of calcified plaque, there are regions of shadowing where the boundary may not be visually obvious. The ICA is often located deep in the neck, and its lumen on ultrasound images contains speckle noise leading to poor contrast at boundary. The geometry and structure of bifurcation and plaque pose a particular challenge for shape based active contour methods. A semiautomatic or automatic algorithm for the segmentation of carotid artery wall must overcome these challenges.

In this work, numerically and theoretically sound 2D and 3D semiautomatic algorithm for the segmentation of lumen-intima boundary (LIB) and adventitial wall boundary (AWB) of atherosclerosis carotid artery with technical details of implementation were presented and evaluated. The segmentation of LIB and AWB is very useful in calculation of vessel wall volume (VWV) and characterization of plaque composition. Quantitative assessment of plaque will help to monitor plaque stabilization by drug therapies and to select patients with high risk plaques so they can be treated invasively while the vast majority of patients with low risk plaques can be treated medically.

The key contributions in this work were the development of a segmentation algorithm for calculating VWV of carotid artery from proximal common carotid to distal internal carotid with a novel stopping criterion and the incorporation of shape of artery (ellipse) as an energy function for accurate segmentation of AWB. The proposed algorithm for segmenting LIB and AWB was evaluated in terms of region-based and boundary-based metrics. The reproducibility of VWV measurement by algorithm and execution time of algorithm were also reported.

Although preliminary validation on 10 subjects showed that the algorithm accurately segmented LIB and AWB, further work is necessary for using it in the clinical settings. The proposed algorithm needs to be validated on more patients data using CT angiography images and endarterectomy. It is also important to know the performance of the proposed algorithm in images captured by different manufacturer US machines.

One of the important stages of the algorithm is the initialization of points on the boundary by manual observers. The performance of the algorithm depends on the stopping boundary which is generated from initial points. In current framework of algorithm, points were initialized by observers at an interslice distance of 4mm and initialization in other slices were done by interpolation. In future, texture based image characteristics and image information from other plane will be used for the initialization purposes. It will reduce the variability due to manual initialization. To increase segmentation accuracy of AWB, texture based energy function will be added to the current distance regularized level set frame work.

In conclusion, the proposed algorithm represents a viable approach for the segmentation of LIB and AWB of carotid artery using 3D ultrasound imaging despite many improvements can be devised to the proposed algorithm. Given the quality of the available data, quantitative evaluation of proposed algorithm shows that proposed algorithm is successful in segmenting LIB and AWB boundary of carotid artery. The proposed algorithm can be helpful in clinical care for fast and economical monitoring of 3D plaque progression and regression during therapy.

Bibliography

Bibliography

[1] G. Treece, R. Prager, and A. Gee, "The stradwin 3d ultrasound acquisition and visualization system."

[2] World health organization. the atlas of heart diseas. (Accessed: 15 March 2014). [Online]. Available: http://www.who.int/cardiovascular_diseases/en/cvd_atlas_16_death_from_stroke.pdf

[3] S. Murphy, J. Xu, and K. Kochanek, "Deaths: preliminary data for 2010," *National vital statistics reports*, vol. 60, no. 4, pp. 1–68, 2012.

[4] "Centers of disease control and prevention [homepage on the internet]," http://www.cdc.gov, atlanta: Centers of Disease Control and Prevention; [cited 2010 Mar 17].

[5] V. Roger, A. Go, D. Lloyd-Jones, E. Benjamin, J. Berry, W. Borden, D. Bravata, S. Dai, E. Ford, C. Fox *et al.*, "Heart disease and stroke statistics2012 update a report from the american heart association," *Circulation*, vol. 125, no. 1, pp. e2–e220, 2012.

[6] M. M. S. M. D. Geoffrey A Donnan, Marc Fisher, "Stroke," *The Lancet*, vol. 371, pp. 1612–1623, 2008.

[7] S. Chaturvedi, A. Bruno, T. Feasby, R. Holloway, O. Benavente, S. Cohen, R. Cote, D. Hess, J. Saver, J. Spence *et al.*, "Carotid endarterectomyan evidence-based review report of the therapeutics and technology assessment subcommittee of the american academy of neurology," *Neurology*, vol. 65, no. 6, pp. 794–801, 2005.

[8] D. Small, "George lyman duff memorial lecture. progression and regression of atherosclerotic lesions. insights from lipid physical biochemistry." *Arteriosclerosis, Thrombosis, and Vascular Biology*, vol. 8, no. 2, pp. 103–129, 1988.

[9] F. H. Epstein and R. Ross, "Atherosclerosisan inflammatory disease," *New England journal of medicine*, vol. 340, no. 2, pp. 115–126, 1999.

[10] P. Libby, P. M. Ridker, and A. Maseri, "Inflammation and atherosclerosis," *Circulation*, vol. 105, no. 9, pp. 1135–1143, 2002.

[11] R. Virmani, A. Burke, E. Ladich, and F. D. Kolodgie, "Pathology of carotid artery atherosclerotic disease," *Carotid Disease. 1st ed. Cambridge University Press, Cambridge, United Kingdom*, pp. 1–2, 2007.

[12] N. A. S. C. E. T. Collaborators *et al.*, "Beneficial effect of carotid endarterectomy in symptomatic patients with high-grade carotid stenosis." *The New England journal of medicine*, vol. 325, no. 7, p. 445, 1991.

[13] C. Warlow, "Mrc european carotid surgery trial: interim results for symptomatic patients with severe (70-99%) or with mild (0-29%) carotid stenosis," *The Lancet*, vol. 337, no. 8752, pp. 1235–1243, 1991.

[14] B. Farrell, A. Fraser, P. Sandercock, J. Slattery, and C. Warlow, "Randomised trial of endarterectomy for recently symptomatic carotid stenosis: final results of the mrc european carotid surgery trial (ecst)," *Lancet*, vol. 351, no. 9113, pp. 1379–1387, 1998.

[15] H. J. Barnett, D. W. Taylor, M. Eliasziw, A. J. Fox, G. G. Ferguson, R. B. Haynes, R. N. Rankin, G. P. Clagett, V. C. Hachinski, D. L. Sackett *et al.*, "Benefit of carotid endarterectomy in patients with symptomatic moderate or severe stenosis," *New England Journal of Medicine*, vol. 339, no. 20, pp. 1415–1425, 1998.

[16] M. D. Walker, J. R. Marler, M. Goldstein, P. A. Grady, J. F. Toole, W. H. Baker, J. E. Castaldo, L. E. Chambless, W. S. Moore, J. T. Robertson *et al.*, "Endarterectomy for asymptomatic carotid artery stenosis," *JAMA*, vol. 273, no. 18, pp. 1421–1428, 1995.

[17] S. W. Mayo, J. Eldrup-Jorgensen, F. Lucas, D. E. Wennberg, and C. E. Bredenberg, "Carotid endarterectomy after nascet and acas: a statewide study," *Journal of vascular surgery*, vol. 27, no. 6, pp. 1017–1023, 1998.

[18] B. Young, W. S. Moore, J. T. Robertson, J. F. Toole, C. B. Ernst, S. N. Cohen, J. P. Broderick, R. J. Dempsey, J. D. Hosking *et al.*, "An analysis of perioperative surgical mortality and morbidity in the asymptomatic carotid atherosclerosis study," *Stroke*, vol. 27, no. 12, pp. 2216–2224, 1996.

[19] P. M. Rothwell, "Acst: which subgroups will benefit most from carotid endarterectomy?" *The Lancet*, vol. 364, no. 9440, pp. 1122–1123, 2004.

[20] M. J. Koelemay, P. J. Nederkoorn, J. B. Reitsma, and C. B. Majoie, "Systematic review of computed tomographic angiography for assessment of carotid artery disease," *Stroke*, vol. 35, no. 10, pp. 2306–2312, 2004.

[21] H. R. Underhill, W. S. Kerwin, T. S. Hatsukami, and C. Yuan, "Automated measurement of mean wall thickness in the common carotid artery by mri: A comparison to intima-media thickness by b-mode ultrasound," *Journal of Magnetic Resonance Imaging*, vol. 24, no. 2, pp. 379–387, 2006.

[22] T. Saam, M. Ferguson, V. Yarnykh, N. Takaya, D. Xu, N. Polissar, T. Hatsukami, and C. Yuan, "Quantitative evaluation of carotid plaque composition by in vivo mri," *Arteriosclerosis, thrombosis, and vascular biology*, vol. 25, no. 1, pp. 234–239, 2005.

[23] D. Pretorius, T. Nelson, and J. Jaffe, "3-dimensional sonographic analysis based on color flow doppler and gray scale image data: a preliminary report." *Journal of ultrasound in medicine*, vol. 11, no. 5, pp. 225–232, 1992.

[24] G. L. Moneta, J. M. Edwards, G. Papanicolaou, T. Hatsukami, L. M. Taylor Jr, D. E. Strandness Jr, and J. M. Porter, "Screening for asymptomatic internal carotid artery stenosis: duplex criteria for discriminating 60% to 99% stenosis," *Journal of vascular surgery*, vol. 21, no. 6, pp. 989–994, 1995.

[25] M. L. Bots, A. W. Hoes, P. J. Koudstaal, A. Hofman, and D. E. Grobbee, "Common carotid intima-media thickness and risk of stroke and myocardial infarction: the rotterdam study," *Circulation*, vol. 96, no. 5, pp. 1432–1437, 1997.

[26] D. Baldassarre, M. Amato, A. Bondioli, C. R. Sirtori, and E. Tremoli, "Carotid artery intima-media thickness measured by ultrasonography in normal clinical practice correlates well with atherosclerosis risk factors," *Stroke*, vol. 31, no. 10, pp. 2426–2430, 2000.

[27] G. K. Owens, "Control of hypertrophic versus hyperplastic growth of vascular smooth muscle cells," *American Journal of Physiology-Heart and Circulatory Physiology*, vol. 257, no. 6, pp. H1755–H1765, 1989.

[28] M. Hennerici, H. Baezner, and M. Daffertshofer, "Ultrasound and arterial wall disease," *Cerebrovascular Diseases*, vol. 17, no. Suppl. 1, pp. 19–33, 2003.

[29] J. D. Spence, M. Eliasziw, M. DiCicco, D. G. Hackam, R. Galil, and T. Lohmann, "Carotid plaque area a tool for targeting and evaluating vascular preventive therapy," *Stroke*, vol. 33, no. 12, pp. 2916–2922, 2002.

[30] C. D. Ainsworth, C. C. Blake, A. Tamayo, V. Beletsky, A. Fenster, and J. D. Spence, "3D ultrasound measurement of change in carotid plaque volume a tool for rapid evaluation of new therapies," *Stroke*, vol. 36, no. 9, pp. 1904–1909, 2005.

[31] A. Krasinski, B. Chiu, J. D. Spence, A. Fenster, and G. Parraga, "Three-dimensional ultrasound quantification of intensive statin treatment of carotid atherosclerosis," *Ultrasound in medicine & biology*, vol. 35, no. 11, pp. 1763–1772, 2009.

[32] M. Egger, J. Spence, A. Fenster, and G. Parraga, "Validation of 3d ultrasound vessel wall volume: an imaging phenotype of carotid atherosclerosis," *Ultrasound in medicine & biology*, vol. 33, no. 6, pp. 905–914, 2007.

[33] E. Ukwatta, J. Awad, A. D. Ward, D. Buchanan, J. Samarabandu, G. Parraga, and A. Fenster, "Three-dimensional ultrasound of carotid atherosclerosis: Semiautomated segmentation using a level set-based method," *Medical Physics*, vol. 38, p. 2479, 2011.

[34] B. Chiu, M. Egger, J. D. Spence, G. Parraga, and A. Fenster, "Quantification of carotid vessel wall and plaque thickness change using 3d ultrasound images," *Medical physics*, vol. 35, p. 3691, 2008.

[35] M. Egger, B. Chiu, J. D. Spence, A. Fenster, and G. Parraga, "Mapping spatial and temporal changes in carotid atherosclerosis from three-dimensional ultrasound images," *Ultrasound in medicine & biology*, vol. 34, no. 1, pp. 64–72, 2008.

[36] B. Chiu, V. Beletsky, J. D. Spence, G. Parraga, and A. Fenster, "Analysis of carotid lumen surface morphology using three-dimensional ultrasound imaging," *Physics in medicine and biology*, vol. 54, no. 5, p. 1149, 2009.

[37] P. Abolmaesumi, M. R. Sirouspour, and S. Salcudean, "Real-time extraction of carotid artery contours from ultrasound images," in *Computer-Based Medical Systems, 2000. CBMS 2000. Proceedings. 13th IEEE Symposium on*. IEEE, 2000, pp. 181–186.

[38] F. Mao, J. Gill, D. Downey, and A. Fenster, "Segmentation of carotid artery in ultrasound images: Method development and evaluation technique," *Medical physics*, vol. 27, p. 1961, 2000.

[39] A. Zahalka and A. Fenster, "An automated segmentation method for three-dimensional carotid ultrasound images," *Physics in medicine and biology*, vol. 46, no. 4, p. 1321, 2001.

[40] J. D. Gill, H. M. Ladak, D. A. Steinman, and A. Fenster, "Accuracy and variability assessment of a semiautomatic technique for segmentation of the carotid arteries from three-dimensional ultrasound images," *Medical physics*, vol. 27, p. 1333, 2000.

[41] J. Guerrero, S. E. Salcudean, J. A. McEwen, B. A. Masri, and S. Nicolaou, "Real-time vessel segmentation and tracking for ultrasound imaging applications," *Medical Imaging, IEEE Transactions on*, vol. 26, no. 8, pp. 1079–1090, 2007.

[42] I. Solovey, "Segmentation of 3d carotid ultrasound images using weak geometric priors," 2010.

[43] E. Ukwatta, J. Awad, A. D. Ward, D. Buchanan, G. Parraga, and A. Fenster, "Coupled level set approach to segment carotid arteries from 3d ultrasound images," in *Biomedical Imaging: From Nano to Macro, 2011 IEEE International Symposium on*. IEEE, 2011, pp. 37–40.

[44] X. Yang, J. Jin, W. He, M. Yuchi, and M. Ding, "Segmentation of the common carotid artery with active shape models from 3d ultrasound images," in *Proc. of SPIE Vol*, vol. 8315, 2012, pp. 83 152H–1.

[45] E. Ukwatta, J. Yuan, D. Buchanan, B. Chiu, J. Awad, W. Qiu, G. Parraga, and A. Fenster, "Three-dimensional segmentation of three-dimensional ultrasound carotid atherosclerosis using sparse field level sets," *Medical physics*, vol. 40, p. 052903, 2013.

[46] A. M. A. Lorza, D. D. Carvalho, J. Petersen, A. C. van Dijk, A. van der Lugt, W. J. Niessen, S. Klein, and M. de Bruijne, "Carotid artery lumen segmentation in 3d free-hand ultrasound images using surface graph cuts," in *Medical Image Computing and Computer-Assisted Intervention–MICCAI 2013*. Springer, 2013, pp. 542–549.

[47] L. D. Cohen and I. Cohen, "Finite-element methods for active contour models and balloons for 2-d and 3-d images," *Pattern Analysis and Machine Intelligence, IEEE Transactions on*, vol. 15, no. 11, pp. 1131–1147, 1993.

[48] F. Leymarie and M. D. Levine, "Tracking deformable objects in the plane using an active contour model," *Pattern Analysis and Machine Intelligence, IEEE Transactions on*, vol. 15, no. 6, pp. 617–634, 1993.

[49] Y. Y. Wong, P. C. Yuen, and C. S. Tong, "Contour length terminating criterion for snake model," *Pattern Recognition*, vol. 31, no. 5, p. 597606, 1998.

[50] Y. Yuan, M. L. Giger, H. Li, K. Suzuki, and C. Sennett, "A dual-stage method for lesion segmentation on digital mammograms," *Medical physics*, vol. 34, pp. 4180–4193, 2007.

[51] K. Chaudhury and K. Ramakrishnan, "Stability and convergence of the level set method in computer vision," *Pattern Recognition Letters*, vol. 28, no. 7, pp. 884–893, 2007.

[52] M. Dubuisson and A. Jain, "A modified hausdorff distance for object matching," in *Pattern Recognition, 1994. Vol. 1-Conference A: Computer Vision & Image Processing., Proceedings of the 12th IAPR International Conference on*, vol. 1. IEEE, 1994, pp. 566–568.

[53] M. M. Hossain, K. AlMuhanna, L. Zhao, B. Lal, and S. Sikdar, "Semiautomatic segmentation of atherosclerotic carotid artery lumen using 3d ultrasound imaging," in *SPIE Medical Imaging*. International Society for Optics and Photonics, 2013, pp. 86 694A–86 694A.

[54] A. Fenster, D. B. Downey, and H. N. Cardinal, "Three-dimensional ultrasound imaging," *Physics in medicine and biology*, vol. 46, no. 5, p. R67, 2001.

[55] B. Zhuang, V. Shamdasani, S. Sikdar, R. Managuli, and Y. Kim, "Real-time 3-d ultrasound scan conversion using a multicore processor," *Information Technology in Biomedicine, IEEE Transactions on*, vol. 13, no. 4, pp. 571–574, 2009.

[56] C. Li, C. Xu, C. Gui, and M. D. Fox, "Distance regularized level set evolution and its application to image segmentation," *Image Processing, IEEE Transactions on*, vol. 19, no. 12, pp. 3243–3254, 2010.

[57] M. P. Dubuisson and A. K. Jain, "A modified hausdorff distance for object matching," in *Pattern Recognition, 1994. Vol. 1-Conference A: Computer Vision & Image Processing., Proceedings of the 12th IAPR International Conference on*, vol. 1, 1994, pp. 566–568.

[58] Y. Zimmer, S. Akselrod, and R. Tepper, "The distribution of the local entropy in ultrasound images," *Ultrasound in medicine & biology*, vol. 22, no. 4, pp. 431–439, 1996.

[59] Y. Yu and S. T. Acton, "Speckle reducing anisotropic diffusion," *Image Processing, IEEE Transactions on*, vol. 11, no. 11, pp. 1260–1270, 2002.

[60] A. Aksel, R. L. Janiczek, J. A. Hossack, B. A. French, and S. T. Acton, "Ultrasound myocardial tracking with speckle reducing anisotropic diffusion assisted initialization," in *Image Processing, 2006 IEEE International Conference on*. IEEE, 2006, pp. 1945–1948.

[61] Q. Sun, J. A. Hossack, J. Tang, and S. T. Acton, "Speckle reducing anisotropic diffusion for 3d ultrasound images," *Computerized Medical Imaging and Graphics*, vol. 28, no. 8, pp. 461–470, 2004.

[62] S. Osher and J. A. Sethian, "Fronts propagating with curvature-dependent speed: algorithms based on hamilton-jacobi formulations," *Journal of computational physics*, vol. 79, no. 1, pp. 12–49, 1988.

[63] J. A. Noble and D. Boukerroui, "Ultrasound image segmentation: a survey," *Medical Imaging, IEEE Transactions on*, vol. 25, no. 8, pp. 987–1010, 2006.

[64] S. Osher and R. Fedkiw, *Level set methods and dynamic implicit surfaces*. Springer, 2003, vol. 153.

[65] D. Peng, B. Merriman, S. Osher, H. Zhao, and M. Kang, "A pde-based fast local level set method," *Journal of Computational Physics*, vol. 155, no. 2, pp. 410–438, 1999.

[66] S. Lankton and A. Tannenbaum, "Localizing region-based active contours," *Image Processing, IEEE Transactions on*, vol. 17, no. 11, pp. 2029–2039, 2008.

[67] T. F. Chan and L. A. Vese, "Active contours without edges," *Image Processing, IEEE Transactions on*, vol. 10, no. 2, pp. 266–277, 2001.

[68] J. Awad, A. Owrangi, L. Villemaire, E. ORiordan, G. Parraga, and A. Fenster, "Three-dimensional lung tumor segmentation from x-ray computed tomography using sparse field active models," *Medical physics*, vol. 39, no. 2, pp. 851–865, 2012.

[69] O. Van Kaick, G. Hamarneh, H. Zhang, and P. Wighton, "Contour correspondence via ant colony optimization," in *Computer Graphics and Applications, 2007. PG'07. 15th Pacific Conference on*. IEEE, 2007, pp. 271–280.

[70] P. W. Stratford, "Getting more from the literature: estimating the standard error of measurement from reliability studies," *Physiotherapy Canada*, vol. 56, no. 1, pp. 27–30, 2004.

[71] E. Domholdt, *Rehabilitation research: principles and applications*. Elsevier Saunders St. Louisˆ eMo Mo, 2005, vol. 11830.

[72] D. P. Huttenlocher, G. A. Klanderman, and W. J. Rucklidge, "Comparing images using the hausdorff distance," *Pattern Analysis and Machine Intelligence, IEEE Transactions on*, vol. 15, no. 9, pp. 850–863, 1993.

[73] V. Chalana and Y. Kim, "A methodology for evaluation of boundary detection algorithms on medical images," *Medical Imaging, IEEE Transactions on*, vol. 16, no. 5, pp. 642–652, 1997.

[74] W. W. Daniel, "Applied nonparametric statistics," 1990.

[75] A. Nicolaides, K. W. Beach, E. Kyriacou, and C. S. Pattichis, *Ultrasound and Carotid Bifurcation Atherosclerosis*. Springer, 2011.

[76] D. G. Altman and J. M. Bland, "Measurement in medicine: the analysis of method comparison studies," *The statistician*, pp. 307–317, 1983.

Curriculum Vitae

Md Murad hossain received his Bachelor of Science in Electrical and Electronic Engineering from the Islamic University of Technology (IUT), Bangladesh in 2009. He joined IUT as a Lecturer where he conducted labs and electrical circuits course. He started his Master of Science in Electrical Engineering at George Mason University in 2011. He will start his PhD in Biomedical Engineering at jooint program of University of North Carolina, chapel Hill and North Carolina State University. He is interested in doing research on image processing, pattern recognition, and ultrasound imaging.